EQUILIBRIUM, STABILITY AND
ORBITAL EVOLUTION
OF CLOSE BINARY SYSTEMS

Dong Lai [1]

Center for Radiophysics and Space Research, Cornell University, Ithaca, NY 14853

Frederic A. Rasio [2]

Institute for Advanced Study, Princeton, NJ 08540

and

Stuart L. Shapiro [3]

Center for Radiophysics and Space Research, Cornell University, Ithaca, NY 14853

ABSTRACT

We present a new analytic study of the equilibrium and stability properties of close binary systems containing polytropic components. Our method is based on the use of ellipsoidal trial functions in an energy variational principle. We consider both synchronized and nonsynchronized systems, constructing the compressible generalizations of the classical Darwin and Darwin-Riemann configurations. Our method can be applied to a wide variety of binary models where the stellar masses, radii, spins, entropies, and polytropic indices are all allowed to vary over wide ranges and independently for each component. We find that both secular and dynamical instabilities can develop before a Roche limit or contact is reached along a sequence of models with decreasing binary separation. High incompressibility always makes a given binary system more susceptible to these instabilities, but the dependence on the mass ratio is more complicated. As simple applications, we construct models of double degenerate systems and of low-mass main-sequence-star binaries. We also discuss the orbital evolution of close binary systems under the combined influence of fluid viscosity and secular angular momentum losses from processes like gravitational radiation. We show that the existence of global fluid instabilities can have a profound effect on the terminal evolution of coalescing binaries. The validity of our analytic solutions is examined by means of detailed comparisons with the results of recent numerical fluid calculations in three dimensions.

Subject headings: hydrodynamics — instabilities — stars: general — stars: binaries: close

1. INTRODUCTION

Essentially all recent theoretical work on close binary systems has been done in the Roche approximation, where the noncompact components are modeled as massless gas in hydrostatic equilibrium in the effective potential of a point-mass system (see, e.g., Kopal 1959). This model applies well to very compressible objects with centrally concentrated mass profiles, such as giants and early-type main-sequence stars. Some theoretical work has also been done in the completely opposite limit of binaries containing a self-gravitating, *incompressible* fluid (see Chandrasekhar

---

[1] Department of Physics, Cornell University.
[2] Hubble Fellow.
[3] Departments of Astronomy and Physics, Cornell University.

1969, and references therein; see also Hachisu & Eriguchi 1984b). An essential new result found in the incompressible case is that the hydrostatic equilibrium solutions for sufficiently close binaries can become *globally unstable*. The main goal of this paper is to explore how far into the compressible domain these instabilities persist. We parametrize compressibility by adopting a polytropic equation of state and varying the polytropic index.

In a previous paper (Lai, Rasio, & Shapiro 1993a, hereafter LRS1), we have presented a comprehensive analytic study of ellipsoidal figures of equilibrium for both single rotating polytropes and polytropes in binary systems. We have been able to provide compressible generalizations for all the classical incompressible solutions (Chandrasekhar 1969, hereafter Ch69). Our approach is based on the use of an energy variational principle to construct approximate equilibrium solutions and study their stability. Some applications of our results to the problem of binary coalescence have been discussed in Lai, Rasio, & Shapiro (1993b, c; hereafter LRS2 and LRS3). As in Ch69, we have so far treated only binary systems containing one star (extended component) in orbit around a point-mass companion (as in the classical Roche problem) or two identical stars (as in the classical Darwin problem). We have also treated some nonsynchronized generalizations of these cases (the so-called Roche-Riemann and Darwin-Riemann configurations; cf. Aizenman 1968).

In this paper, we extend our study to the most general case of binary systems containing two different polytropes. Specifically, we allow the two components to have different masses, radii, entropies, polytropic indices, and, for nonsynchronized systems, spins. We refer to these binary models as general Darwin-Riemann configurations. Earlier work based on the tensor-virial method suggested that Darwin-Riemann binary models could be constructed only for the particular cases where the mass ratio is either unity or tends to zero (Ch69). Instead, we show here that our energy variational method can be generalized quite naturally to construct binary models with arbitrary, unequal-mass components.

The usefulness of our analytic approach lies in its simplicity. Numerical codes can be used to construct very accurate hydrostatic equilibrium configurations in three dimensions, but they require appreciable computer resources. By contrast, to obtain an equilibrium model with our method simply involves solving a set of algebraic equations, a task that can be performed on a workstation in seconds. As a result, we can explore a wide variety of possible binary models. In addition, our analytic treatment can provide physical insight into difficult issues of global stability that are easily missed when using multidimensional numerical calculations. In our analytic treatment, instabilities are identified simply from turning points appearing along sequences of equilibrium configurations. Specifically, along an equilibrium sequence parametrized by the binary separation r, the onset of instability occurs at a point $r = r_m$ where the total energy E and angular momentum J of the system simultaneously attain a *minimum*. We showed in LRS1 that such a turning point along a binary equilibrium sequence marks the onset of instability. Depending on the nature of the equilibrium sequence considered, the instability can be either secular or dynamical.

As far as we are aware, *dynamical instabilities* of close binary systems have never been discussed before, except in the context of the classical Darwin problem for incompressible fluids (Tassoul 1975; Chandrasekhar 1975). The existence of a minimum of the total angular momentum J at some $r = r_m$ has been noted before in simple models of *synchronized* (i.e., uniformly rotating) binary systems (Counselman 1973; Hut 1980). In synchronized systems, the minimum comes essentially from the angular momentum and energy of the spins, which increase as r decreases. In this case the minimum marks the onset of *secular instability*. Counselman (1973) and Hut (1980) have discussed this secular instability for binary systems where the two stars can be represented by rigid spheres. This can apply only to systems with extreme mass ratios, such as planet-satellite systems, which have $r_m/R \gg 1$, where R is the radius of the more extended component. In most binary systems, however, we find that $r_m/R \gtrsim 1$ and the tidal distortion of the more extended

component cannot be neglected.

Our results have important implications for a variety of astrophysical systems of great current interest. Both secular and dynamical instabilities can lead to an acceleration of the orbital decay of a close binary, and, eventually, drive the two stars to a rapid coalescence. Close neutron star binaries are most important sources of gravitational radiation in the Universe, and are the primary targets for the LIGO project (Abramovici et al. 1992). The coalescence of two neutron stars is at the basis of numerous models of γ-ray bursters (see Narayan, Paczyński, & Piran 1992 and references therein). The consequences of fluid instabilities for the final orbital decay of neutron star binaries and the corresponding gravitational radiation waveforms have been explored in LRS3. Double white dwarf systems are now generally thought to be the progenitors of type Ia supernovae (Iben & Tutukov 1984). They are also promising sources of low-frequency gravitational waves that should be easily detectable by future space-based interferometers (Evans, Iben, & Smarr 1987). In addition to producing supernovae, the coalescence of two white dwarfs may also lead in certain cases to the formation by gravitational collapse of an isolated millisecond pulsar (Chen & Leonard 1993) or the formation of blue subdwarf stars in globular clusters (Bailyn 1993). In the case of coalescing magnetized white dwarfs, a neutron star with extremely high magnetic field may form, and such an object has also been proposed as a source of γ-ray bursts (Usov 1992). Coalescing main-sequence star binaries are the likely progenitors of blue stragglers in stellar clusters (Mateo et al. 1990). Contact main-sequence star binaries are also directly observed as W UMa systems. The requirement that these systems live long enough to be observed during a contact phase (i.e., remain stable) could place important constraints on theoretical models of their interior structure (Rasio 1993). Finally, mass-transfer systems, such as X-ray binaries and cataclysmic variables, could also be affected by instabilities if the donor star is sufficiently incompressible or massive. A version of the secular instability described here was recently considered by Levine et al. (1991, 1993) in the context of the orbital evolution of LMC X-4 and SMC X-1.

This paper is organized as follows. In §2 we present our analytic method of constructing equilibrium binary models. In §3 we discuss the various stability and Roche limits for these models. We then study in §4 the general characteristics of simple models for astrophysical systems containing white dwarfs, brown dwarfs, planets, main-sequence stars, and neutron stars. In §5 we compare some of our analytic results with those of recent numerical calculations. In §6 we discuss the secular orbital evolution of close binaries in the presence of dissipation.

2. COMPRESSIBLE DARWIN-RIEMANN MODELS

In this section, we describe our energy variational method to construct general Darwin-Riemann equilibrium models. In §2.1 we briefly summarize the basic ideas and assumptions. More details about the method in general, as well as many other applications, can be found in LRS1. The equilibrium equations for compressible Darwin-Riemann configurations are derived in §2.2. The method of solution and the construction of equilibrium sequences are discussed in §2.3.

2.1 Basic Assumptions

Consider an isolated, self-gravitating fluid system in steady state. The system is characterized by conserved global quantities such as its total mass M and total angular momentum J. The total energy the system (not necessarily in equilibrium) can always be written as a functional of the fluid density and velocity fields $\rho(\mathbf{x})$ and $\mathbf{v}(\mathbf{x})$. In principle, an equilibrium configuration can be determined by extremizing this energy functional with respect to all variations of $\rho(\mathbf{x})$ and $\mathbf{v}(\mathbf{x})$ that leave the conserved quantities unchanged. The basic idea in our method is to replace the infinite number of degrees of freedom contained in $\rho(\mathbf{x})$ and $\mathbf{v}(\mathbf{x})$ by a limited number of parameters

$\alpha_1,\ \alpha_2,\ldots$, in such a way that the total energy becomes a function of these parameters,

$$E = E(\alpha_1, \alpha_2, \ldots; M, J, \ldots), \tag{2.1}$$

An equilibrium configuration is then determined by extremizing the energy according to

$$\frac{\partial E}{\partial \alpha_i} = 0, \quad i = 1, 2, \ldots \tag{2.2}$$

where the partial derivatives are taken holding $M, J, \ldots$ constant.

An expression like (2.1) can be written down for the total energy of a binary star system provided that enough simplifying assumptions are made. In this paper, we consider only binaries in circular orbit and we adopt a polytropic equation of state for the fluid. Under the combined effects of centrifugal and tidal forces, the stars assume nonspherical shapes. We model these shapes as triaxial ellipsoids. Specifically, we assume that the surfaces of constant density within each star can be modeled as *self-similar ellipsoids*. The geometry is then completely specified by the three principle axes of the outer surface. Furthermore, we assume that the density profile $\rho(m)$ inside each star, where m is the mass interior to an isodensity surface, is identical to that of a *spherical* polytrope with the same volume. The velocity field of the fluid is modeled as either uniform rotation (corresponding to the case of a synchronized binary systems), or uniform *vorticity* (for nonsynchronized systems). The vorticity vector is assumed to be everywhere parallel to the orbital rotation axis.

For an isolated rotating star, these assumptions are satisfied *exactly* when the fluid is incompressible (polytropic index $n = 0$), in which case the true equilibrium configuration is a homogeneous ellipsoid (cf. Ch69). For a star in a binary system, our assumptions are strictly valid in the incompressible limit only if we truncate the tidal interaction to quadrupole order. We adopt this quadrupole-order truncation of the interaction potential in this paper. For polytropes with $n \neq 0$, our assumptions are only satisfied approximately. In that case our two-ellipsoid models should be considered as trial functions used in combination with the energy variational principle to find approximate equilibrium solutions.

2.2 Derivation of the Equilibrium Equations

We consider a binary system containing two polytropes of mass M and M' in circular orbit around each other. Throughout this paper unprimed quantities refer to the star of mass M and primed quantities refer to the star of mass M'. Following Ch69, we denote the mass ratio as $p \equiv M/M'$. The density and pressure are related by

$$P = K\rho^{(1+1/n)}, \quad P' = K'\rho'^{\,(1+1/n')}. \tag{2.3}$$

Note that we allow the two stars to have different polytropic indices ($n \neq n'$) and different polytropic constants ($K \neq K'$). This allows us to model realistically a variety of astrophysical systems where the two stars have different masses and radii (see §4). The binary separation is denoted by r, and the principal axes of the two ellipsoids by a_1, a_2, a_3, and a_1', a_2', a_3'. The orientation is such that a_1 and a_1' are measured along the binary axis, a_2 and a_2' in the direction of the orbital motion, and a_3 and a_3' along the rotation axis. In place of the three principle axes a_i, it is often convenient to introduce as independent variables the central density ρ_c, and two oblateness parameters defined as

$$\lambda_1 \equiv \left(\frac{a_3}{a_1}\right)^{2/3}, \quad \lambda_2 \equiv \left(\frac{a_3}{a_2}\right)^{2/3}. \tag{2.4}$$

Similarly we can introduce ρ_c', λ_1' and λ_2' in place of the three a_i'. Thus the seven independent variables which specify the structure of our models are $\{\alpha_i, \ i = 1, \cdots, 7\} = \{r, \ \rho_c, \ \lambda_1, \ \lambda_2, \ \rho_c', \ \lambda_1', \ \lambda_2'\}$.

2.2.1 Energy Function

We first obtain an expression for the total energy of the system under the assumptions given in §2.1. A detailed derivation for the similar case of Roche-Riemann configurations was given in LRS1 and will not be repeated here. References to key equations in LRS1 are indicated with numbers preceded by an "I". Throughout this section, when two similar expressions can be written for the two stars, we only give the one corresponding to M, the other being obtained trivially by replacing unprimed by primed quantities.

The total internal energy in each star is given by (cf. eq. [I.3.1])

$$U = \int \frac{nP}{\rho} \, dm = k_1 K \rho_c^{1/n} M. \tag{2.5}$$

The self-gravitational potential energy can be written (cf. eq. [I.4.6])

$$W = -\frac{3}{5-n} \frac{GM^2}{R} f = -k_2 GM^{5/3} \rho_c^{1/3} f, \tag{2.6}$$

where we have defined the mean radius $R \equiv (a_1 a_2 a_3)^{1/3}$ and the dimensionless ratio

$$f = f(\lambda_1, \lambda_2) \equiv \frac{A_1 a_1^2 + A_2 a_2^2 + A_3 a_3^2}{2R^2}, \tag{2.7}$$

such that $f = 1$ for a spherical star. The index symbols A_i are defined as in Ch69 (§17),

$$A_i \equiv a_1 a_2 a_3 \int_0^\infty \frac{du}{\Delta(a_i^2 + u)}, \quad \text{with} \quad \Delta^2 = (a_1^2 + u)(a_2^2 + u)(a_3^2 + u). \tag{2.8}$$

They are functions of λ_1 and λ_2 only. In equations (2.5) and (2.6), k_1 and k_2 are dimensionless polytropic structure constants (depending only on n), defined as

$$k_1 \equiv \frac{n(n+1)}{5-n} \xi_1 |\theta'_1|, \quad k_2 \equiv \frac{3}{5-n} \left(\frac{4\pi |\theta'_1|}{\xi_1} \right)^{1/3}, \tag{2.9}$$

where θ and ξ are the usual Lane-Emden variables for a polytrope (see, e.g., Chandrasekhar 1939). Values of k_1 and k_2 for different n are given in Table 1 of LRS1, but they are not needed explicitly for constructing equilibrium solutions.

The fluid velocity field inside each star is modeled exactly as in a Riemann-S ellipsoid (see LRS1, §5, for details). Following Ch69 and LRS1, we introduce a parameter f_R defined as

$$f_R \equiv \frac{\zeta}{\Omega}, \tag{2.10}$$

where Ω is the orbital angular frequency and ζ is the fluid vorticity in the corotating frame,

$$\zeta \equiv (\nabla \times \mathbf{u}) \cdot \mathbf{e}_3 = -\frac{a_1^2 + a_2^2}{a_1 a_2} \Lambda. \tag{2.11}$$

The quantity Λ is the angular frequency of the internal fluid motions. The velocity field in the corotating frame is given by

$$\mathbf{u} = Q_1 x_2 \mathbf{e_1} + Q_2 x_1 \mathbf{e_2},\tag{2.12}$$

where

$$Q_1 = -\frac{a_1^2}{a_1^2 + a_2^2}\zeta = +\frac{a_1}{a_2}\Lambda,$$
$$Q_2 = +\frac{a_2^2}{a_1^2 + a_2^2}\zeta = -\frac{a_2}{a_1}\Lambda.\tag{2.13}$$

Here $\mathbf{e_1}$ is along the binary axis, directed from M to M', $\mathbf{e_2}$ is in the direction of the orbital velocity, and the origin is at the center of mass of M. The fluid velocity in the inertial frame is given by

$$\mathbf{u}^{(0)} = \mathbf{u} + \mathbf{\Omega} \times \mathbf{x},\tag{2.14}$$

and the vorticity in the inertial frame is

$$\zeta^{(0)} \equiv (\nabla \times \mathbf{u}^{(0)}) \cdot \mathbf{e}_3 = (2 + f_R)\,\Omega.\tag{2.15}$$

Uniform rotation (synchronization) corresponds to $f_R = \zeta = \Lambda = 0$. An *irrotational* velocity field is obtained when $f_R = -2$. Note that the two equilibrium figures (the geometric outer shapes of the two stars) always rotate at the orbital angular frequency Ω as seen in the inertial frame.

An expression for the "spin" kinetic energy T_s (i.e., the kinetic energy in internal fluid motions) in the inertial frame can be obtained from equations (2.12)–(2.14). One finds (cf. eq. [I.5.6])

$$T_s = \frac{1}{2}I(\Lambda^2 + \Omega^2) - \frac{2}{5}\kappa_n M a_1 a_2 \Lambda\Omega,\tag{2.16}$$

where

$$I = \frac{1}{5}\kappa_n M(a_1^2 + a_2^2)\tag{2.17}$$

is the moment of inertia. We have defined the dimensionless coefficient

$$\kappa_n \equiv \frac{5}{3}\frac{\int_0^{\xi_1} \theta^n \xi^4 \, d\xi}{\xi_1^4 |\theta'_1|},\tag{2.18}$$

so that $\kappa_n = 1$ for $n = 0$. Values of κ_n are given in Table 1 of LRS1. Similarly, the "spin" angular momentum J_s can be written (cf. eq. [I.5.5])

$$J_s = I\Omega - \frac{2}{5}\kappa_n M a_1 a_2 \Lambda.\tag{2.19}$$

Another important conserved quantity is the fluid circulation C along the equator of the star. Following LRS1 (§5.1) we write

$$\mathcal{C} \equiv \left(-\frac{1}{5\pi}\kappa_n M\right) C = \left(-\frac{1}{5\pi}\kappa_n M\right)\pi a_1 a_2\,\zeta^{(0)} = I\Lambda - \frac{2}{5}\kappa_n M a_1 a_2 \Omega.\tag{2.20}$$

The quantity $\mathcal{C}$ has the dimensions of angular momentum but is proportional to the conserved circulation $C \equiv \pi a_1 a_2 \zeta^{(0)}$. We usually refer to $\mathcal{C}$ itself as the circulation for convenience. Note the complementary roles played by the variables $(J_s, \mathcal{C})$ and (Ω, Λ) (compare expressions [2.19] and [2.20]).

We can now obtain simple expressions for the total kinetic energy and angular momentum in the system. We first rewrite T_s in a form that is more convenient for taking derivatives of the energy function (cf. LRS1, §5.1). We first combine equations (2.19) and (2.20) to derive the result

$$J_s \pm \mathcal{C} = \frac{1}{2} I_\pm (\Omega \pm \Lambda), \tag{2.21}$$

where

$$I_\pm \equiv \frac{2}{5} \kappa_n M (a_1 \mp a_2)^2 = 2 I_s / h_\pm. \tag{2.22}$$

Here $I_s \equiv \frac{2}{5} \kappa_n M R^2$ is the moment of inertia of a sphere with the same volume as the ellipsoid, and $h_\pm \equiv 2R^2/(a_1 \mp a_2)^2$. Using equation (2.21), the kinetic energy T_s can then be expressed as

$$T_s = T_+ + T_-, \tag{2.23}$$

with

$$T_\pm = \frac{1}{8} I_\pm (\Omega \pm \Lambda)^2 = \frac{1}{2 I_\pm} (J_s \pm \mathcal{C})^2. \tag{2.24}$$

The orbital contributions to the total angular momentum and kinetic energy are simply

$$J_o = \mu r^2 \Omega, \quad T_o = \frac{1}{2} \mu \Omega^2 r^2, \tag{2.25}$$

where $\mu = MM'/(M + M')$ is the reduced mass [4]. The total angular momentum and kinetic energy of the system are then given by

$$\begin{aligned} J &= J_s + J_s' + J_o, \\ T &= T_s + T_s' + T_o. \end{aligned} \tag{2.26}$$

Finally, the gravitational interaction energy W_i between the two stars is given, up to quadrupole order, by (see Appendix B of LRS1)

$$W_i = -\frac{GMM'}{r} - \frac{GM}{2r^3}(2I_{11}' - I_{22}' - I_{33}') - \frac{GM'}{2r^3}(2I_{11} - I_{22} - I_{33}), \tag{2.27}$$

where we have defined

$$I_{ij} = \frac{1}{5} \kappa_n M a_i^2 \delta_{ij}, \quad I_{ij}' = \frac{1}{5} \kappa_n' M' a_i'^2 \delta_{ij}. \tag{2.28}$$

The total energy of the system, not necessary in equilibrium, is given by

$$E(r, \rho_c, \lambda_1, \lambda_2, \rho_c', \lambda_1', \lambda_2'; M, M', \mathcal{C}, \mathcal{C}', J) = U + U' + W + W' + T + W_i, \tag{2.29}$$

together with equations (2.5), (2.6), and (2.23)–(2.27).

When extremizing the energy function (2.29) to find equilibrium solutions, we must hold all the conserved quantities M, M', J, $\mathcal{C}$, and $\mathcal{C}'$ constant. Clearly, the form of T given by equations (2.23)–(2.26) is not ideally suited to such a procedure, since its dependence on J, $\mathcal{C}$, and $\mathcal{C}'$ is not

---

[4] Note that the quantity $\mu \equiv GM'/r^3$ introduced in LRS1 is called μ_R in this paper; see below.

explicit. However, using equations (2.21) and (2.26), we can express Ω as a function of the adopted variables $\{\alpha_i\}$ and the conserved quantities as

$$\Omega = \frac{1}{\mu r^2 + I_A}\left[J + \mathcal{C}\left(\frac{h_+ - h_-}{h_+ + h_-}\right) + \mathcal{C}'\left(\frac{h'_+ - h'_-}{h'_+ + h'_-}\right)\right], \tag{2.30}$$

where

$$I_A \equiv \frac{2I_s}{h_+ + h_-} + \frac{2I'_s}{h'_+ + h'_-}. \tag{2.31}$$

Expressions for Λ and Λ' can then be obtained using equation (2.20). In principle, we can substitute these expressions into equation (2.29) and obtain an appropriate expression for T which does not contain Ω, Λ or Λ', and depends only on $\{\alpha_i\}$ and the conserved quantities. Instead, it is more convenient to use the following expression for T,

$$T = \frac{(J_s + \mathcal{C})^2}{2I_+} + \frac{(J_s - \mathcal{C})^2}{2I_-} + \frac{(J - J_s - \mu r^2\Omega + \mathcal{C}')^2}{2I'_+} + \frac{(J - J_s - \mu r^2\Omega - \mathcal{C}')^2}{2I'_-} + \frac{1}{2}\mu r^2\Omega^2. \tag{2.32}$$

Although Ω and J_s appear in this expression, we can treat them as constant parameters when taking a first derivative of E with respect to α_i. This is because $\partial E/\partial\Omega = \partial T/\partial\Omega = 0$ and $\partial E/\partial J_s = 0$, as can be shown easily with the help of equation (2.21).

2.2.2 Equilibrium Conditions

We can now derive the equilibrium conditions (2.2) for a general Darwin-Riemann configuration.

The first equilibrium condition, $\partial E/\partial r = 0$, gives a relation between Ω^2 and r, i.e., the *modified Kepler's law* for the binary (cf. eq. [I.7.6]),

$$\Omega^2 = \frac{G(M + M')}{r^3}(1 + \delta + \delta')$$
$$= \mu_R(1 + p)(1 + \delta + \delta') = \mu_R'(1 + \frac{1}{p})(1 + \delta + \delta'), \tag{2.33}$$

where we have defined

$$\mu_R \equiv GM'/r^3, \qquad \mu_R' \equiv GM/r^3, \tag{2.34}$$

and

$$\delta \equiv \frac{3}{2}\frac{(2I_{11} - I_{22} - I_{33})}{Mr^2}, \qquad \delta' \equiv \frac{3}{2}\frac{(2I'_{11} - I'_{22} - I'_{33})}{M'r^2}. \tag{2.35}$$

Note that for Roche and (equal-mass) Darwin configurations, Ch69 uses $\Omega^2 = \Omega_K^2 = G(M+M')/r^3$ and $\Omega^2 = \Omega_K^2(1 + \delta)$, respectively, whereas our equation (2.33) gives $\Omega^2 = \Omega_K^2(1 + \delta)$ and $\Omega^2 = \Omega_K^2(1 + 2\delta)$. Our value of Ω^2 is more accurate than that used by Ch69 (see LRS1, Appendix C, for a complete discussion). Moreover, in our treatment, there is no restriction on the allowed ratio of M/M'.

The second condition, $\partial E/\partial\rho_c = 0$, leads to the *virial relation* for the star of mass M (cf. eq. [I.7.8]),

$$\frac{3}{n}U + W + 2T_s = -\frac{GMM'}{R}g_t, \tag{2.36}$$

where

$$g_t \equiv \frac{R}{Mr^3}(2I_{11} - I_{22} - I_{33}) = \frac{2}{3}\frac{R}{r}\delta. \tag{2.37}$$

8

From equations (2.5), (2.6), and (2.36), the equilibrium mean radius can be obtained as

$$R = R_o \left[f(\lambda_1, \lambda_2) \left(1 - 2\frac{T_s}{|W|} \right) - \left(\frac{5-n}{3p} \right) g_t \right]^{-n/(3-n)}, \tag{2.38}$$

where R_o is the radius of the spherical polytrope,

$$R_o = \xi_1 \left(\xi_1^2 |\theta_1'| \right)^{-(1-n)/(3-n)} \left[\frac{(n+1)K}{4\pi G} \right]^{n/(3-n)} \left(\frac{M}{4\pi} \right)^{(1-n)/(3-n)}. \tag{2.39}$$

Clearly, the third condition $\partial E/\partial \rho_c' = 0$ gives a similar expression for R',

$$R' = R_o' \left[f(\lambda_1', \lambda_2') \left(1 - 2\frac{T_s'}{|W'|} \right) - \left(\frac{5-n'}{3} \right) p g_t' \right]^{-n'/(3-n')}. \tag{2.40}$$

The fourth and fifth conditions, $\partial E/\partial \lambda_1 = \partial E/\partial \lambda_2 = 0$, together with the virial relation (2.36) can be written in the form (cf. eq. [I.8.4])

$$
\begin{aligned}
-\frac{U}{n} &= \mathcal{M}_{11} + I_{11}(\Omega^2 + 2\mu_R + 2\Omega Q_2) + I_{22}Q_1^2, \\
-\frac{U}{n} &= \mathcal{M}_{22} + I_{22}(\Omega^2 - \mu_R - 2\Omega Q_1) + I_{11}Q_2^2, \\
-\frac{U}{n} &= \mathcal{M}_{33} - \mu_R I_{33},
\end{aligned}
\tag{2.41}
$$

where the Q_i are given in equation (2.13). Here we have introduced the potential-energy tensor (Ch69)

$$\mathcal{M}_{ij} \equiv -2\pi G \bar{\rho} A_i \left(\frac{M a_i^2 \delta_{ij}}{5-n} \right) \qquad \text{(no summation)}, \tag{2.42}$$

such that $W = \mathcal{M}_{ii}$. The quantity $\bar{\rho} \equiv 3M/(4\pi R^3)$ is the mean density. The form of equations (2.41) is identical to that of the corresponding equations for Roche-Riemann configurations (LRS1, §8), but the expression for Ω is different. Equations (2.41) and (2.42) can be used to obtain relations for the principal axes (cf. eqs. [I.8.5], [I.8.6]),

$$
\begin{aligned}
q_n \tilde{\mu}_R \left\{ \frac{Q_1^2}{\mu_R} a_2^2 + \left[2 + (1+p)(1+\delta+\delta') + 2\frac{Q_2\Omega}{\mu_R} \right] a_1^2 + a_3^2 \right\} &= 2(a_1^2 A_1 - a_3^2 A_3), \\
q_n \tilde{\mu}_R \left\{ \frac{Q_2^2}{\mu_R} a_1^2 + \left[(1+p)(1+\delta+\delta') - 1 - \frac{2Q_1\Omega}{\mu_R} \right] a_2^2 + a_3^2 \right\} &= 2(a_2^2 A_2 - a_3^2 A_3),
\end{aligned}
\tag{2.43}
$$

where we have defined

$$q_n \equiv \kappa_n \left(1 - \frac{n}{5} \right), \qquad \tilde{\mu}_R \equiv \frac{\mu_R}{\pi G \bar{\rho}}. \tag{2.44}$$

Using equations (2.13) and (2.33) we see that the quantities Q_i^2/μ_R and $Q_i\Omega/\mu_R$ appearing in equations (2.43) are given by

$$\frac{Q_i^2}{\mu_R} = \hat{Q}_i^2 (1+p)(1+\delta+\delta') f_R{}^2, \qquad \frac{Q_i\Omega}{\mu_R} = \hat{Q}_i (1+p)(1+\delta+\delta') f_R, \tag{2.45}$$

9

where

$$\hat{Q}_1 = -\frac{a_1^2}{a_1^2 + a_2^2}, \qquad \hat{Q}_2 = \frac{a_2^2}{a_1^2 + a_2^2}. \tag{2.46}$$

Here again, the two structure equations (2.43) are very similar to those obtained in the Roche-Riemann case. The similarity results from the fact that, to quadrupole order, each star acts on the other like a point mass. The only real coupling is through Ω: in equations (2.43) and (2.45) we have the factor $(1 + \delta + \delta')$ instead of simply $(1 + \delta)$ in the Roche-Riemann case.

Finally, the last two conditions, $\partial E/\partial\lambda_1' = \partial E/\partial\lambda_2' = 0$, yield two structure equations similar to equations (2.43) for the other component

$$q_n' \, \tilde{\mu}_R' \left\{ \frac{Q_1'^2}{\mu_R'} a_2'^2 + \left[2 + (1 + \frac{1}{p})(1 + \delta + \delta') + 2\frac{Q_2'\Omega}{\mu_R'} \right] a_1'^2 + a_3'^2 \right\} = 2(a_1'^2 A_1' - a_3'^2 A_3'),$$

$$q_n' \, \tilde{\mu}_R' \left\{ \frac{Q_2'^2}{\mu_R'} a_1'^2 + \left[(1 + \frac{1}{p})(1 + \delta + \delta') - 1 - \frac{2Q_1'\Omega}{\mu_R'} \right] a_2'^2 + a_3'^2 \right\} = 2(a_2'^2 A_2' - a_3'^2 A_3'), \tag{2.47}$$

where $q_n' \equiv \kappa_n'(1 - n'/5)$, $\tilde{\mu}_R' \equiv \mu_R'/(\pi G \bar{\rho}')$, and $\bar{\rho}' \equiv 3M'/(4\pi R'^3)$.

The seven equations in (2.33), (2.38), (2.40), (2.43), and (2.47) completely determine the equilibrium configurations. Once the equilibrium values of the seven variables $\{\alpha_i\}$ are determined, the total equilibrium angular momentum can be obtained from equations (2.19), (2.25) and (2.26). Using the virial relations (eq. [2.36] and the corresponding expression for M'), the total equilibrium energy of the system can be written explicitly

$$E_{eq} = E_s + E_s' + \frac{1}{2}\mu r^2 \Omega^2 - \frac{GMM'}{r}$$
$$- \left(\frac{2n+3}{6} \right) \frac{GM'}{r^3} (2I_{11} - I_{22} - I_{33}) - \left(\frac{2n'+3}{6} \right) \frac{GM}{r^3} (2I_{11}' - I_{22}' - I_{33}'), \tag{2.48}$$

where

$$E_s = -\frac{(3-n)GM^2}{(5-n)R} f(\lambda_1, \lambda_2) \left[1 - \left(\frac{3-2n}{3-n} \right) \frac{T_s}{|W|} \right], \tag{2.49}$$

and the expression for E_s' is similar.

2.3 Construction of Equilibrium Sequences

For many astrophysical applications, it is useful to construct sequences of equilibrium configurations with varying binary separation. The onset of instabilities can often be determined by locating turning points along such sequences (see §3). In addition, equilibrium sequences can sometimes be used to describe approximately the orbital evolution of a system driven by some dissipation mechanism (see §6). Different types of equilibrium sequences can be constructed depending on which quantities are held constant along the sequence.

A particularly useful dimensionless ratio that can be used to parametrize an equilibrium sequence is

$$\hat{r} \equiv \frac{r}{a_1 + a_1'}. \tag{2.50}$$

Because a_1 and a_1' can be double-valued functions of r in our models, the quantity $\hat{r}$ does *not*, in general, specify uniquely the absolute separation between the centers of mass of the two components. Instead, it is a measure of how close the surfaces of the two ellipsoids are approaching each other. The usefulness of the definition (2.50) in practice lies in the existence of a *unique*

equilibrium solution for each value of $\hat{r}$ along the sequence. In particular, the *contact solution*, corresponding to the point along a sequence where the surfaces of two ellipsoids are first touching, can be readily determined by setting $\hat{r} = 1$. Physical solutions require $\hat{r} \geq 1$ in our models, since the energy function is calculated for two ellipsoids that do not overlap. Therefore, all our equilibrium sequences terminate at the contact solution.

2.3.1 Darwin-Riemann Sequences

Following traditional practice for sequences of classical Riemann-S and Roche-Riemann ellipsoids (Ch69), we define a Darwin-Riemann sequence as a sequence of Darwin-Riemann configurations along which the quantities f_R and f_R' (cf. eq. [2.10]) are held constant.

Darwin-Riemann sequences are constructed as follows. We adopt units such that $G = M = R_o = 1$ and fix the values of $p = M/M'$, R_o/R_o' (or, equivalently, K/K'), f_R, and f_R' along the sequence. For each value of $1 \leq \hat{r} < \infty$, we solve the equilibrium equations for the variables $(\hat{x}_j) = (\hat{a}_1, \hat{a}_2, \hat{a}_3, \hat{a}_1', \hat{a}_2', \hat{a}_3')$, where $\hat{a}_i \equiv a_i/(a_1 + a_1')$ and $\hat{a}_i' \equiv a_i'/(a_1 + a_1')$. Specifically, we solve the coupled set of algebraic equations numerically by a Newton-Raphson iteration method. The following six functions must vanish simultaneously:

$$F_1 = \hat{a}_1 + \hat{a}_1' - 1,$$

$$F_2 = \frac{R}{R'} - \left(\frac{a_1 a_2 a_3}{a_1' a_2' a_3'}\right)^{1/3}, \quad \text{with } R, R' \text{ given by eqs. [2.38] and [2.40]},$$

$$F_3 = \text{LHS(eq. [2.43a])} - \text{RHS(eq. [2.43a])},$$

$$F_4 = \text{LHS(eq. [2.43b])} - \text{RHS(eq. [2.43b])}, \qquad (2.51)$$

$$F_5 = \text{LHS(eq. [2.47a])} - \text{RHS(eq. [2.47a])},$$

$$F_6 = \text{LHS(eq. [2.47b])} - \text{RHS(eq. [2.47b])}.$$

We use the standard Newton-Raphson algorithm described by Press et al. (1987), except that here the matrix $(\partial F_i/\partial \hat{x}_j)$ needed in every Newton-Raphson iteration must be evaluated numerically by finite difference. An equilibrium solution can be calculated to an accuracy of $\delta a_i/a_i < 10^{-5}$ in ~ 1 CPU second on a Sun SPARC workstation. We start the calculation for a large value of $\hat{r}$, so that spherical stars can be used as an initial guess. As $\hat{r}$ is decreased, we use as initial guess the equilibrium solution previously determined for a slightly larger $\hat{r}$. Once the principal axes are determined, other physical quantities such as E, J, and Ω can then be calculated using the expressions given in §2.2.

From equation (2.29), we can easily prove that the relation

$$dE = \Omega \, dJ + \Lambda \, d\mathcal{C} + \Lambda' \, d\mathcal{C}', \qquad (2.52)$$

(cf. LRS1, Appendix D). must be satisfied along any equilibrium sequence. This provides a convenient check on our numerical results. In particular, for synchronized sequences ($\Lambda = \Lambda' = 0$) and constant-circulation sequences (see below), we must have $dE = \Omega \, dJ$ (cf. Ostriker & Gunn 1969).

2.3.2 Compressible Darwin Sequences

The classical Darwin problem (Ch69) concerns two identical, incompressible objects ($n = 0$) in a *synchronized* (uniformly rotating) system. Here we generalize the classical Darwin configurations by allowing for compressibility as well as nonidentical components. The synchronized Darwin sequences can be constructed as a special case of the general Darwin-Riemann sequences where

we set $f_R = f_R{}' = 0$. In this case we have $\Lambda = \Lambda' = 0$ and there are no internal fluid motions in the corotating frame of the binary. As an illustration, Figure 1 shows the variation of the total equilibrium energy E (eq. [2.48]), total angular momentum J, and orbital frequency Ω along selected Darwin sequences. Note that the kinetic energy (eq. [2.32]) for Darwin configurations can be written simply

$$T = \frac{1}{2}(\mu r^2 + I + I')\,\Omega^2 = \frac{J^2}{2\,(\mu r^2 + I + I')}. \tag{2.53}$$

Synchronization can be achieved in close binaries if there is a large enough effective viscosity to maintain the tidal coupling between the spins and the orbital motion. This is expected to be the case for the majority of close binaries with the possible exception of double neutron star systems (see §4.3). If there is another dissipation mechanism, e.g., gravitational radiation, that drives orbital decay on a time scale much longer than the viscous dissipation time scale, then we can expect the system to evolve along a synchronized equilibrium sequence (see §6).

2.3.3 Constant-Circulation Sequences

In the opposite limit, when viscosity is completely negligible, a systen whose orbit is decaying because of gravitational radiation evolves along a sequence of configurations with constant $\mathcal{C}$ and $\mathcal{C}'$. This is because the gravitational radiation reaction forces conserve the fluid circulation (Miller 1974). Constant-circulation sequences may describe the orbital evolution of coalescing neutron star binaries (Kochanek 1992).

The value of $\mathcal{C}$ is set by the spin angular frequency Ω_s of M when the binary separation is large; similarly for $\mathcal{C}'$. From equation (2.33) we see that, for large r, we may set $\Omega^2 = G(M + M')/r^3$, and we then have (cf. eqs. [2.19] and [2.20])

$$\begin{aligned} J &\to \mu r^2 \Omega - I\Lambda - I'\Lambda' = \mu r^2 \Omega + I\Omega_s + I'\Omega_s', \\ \mathcal{C} &\to I\Lambda = -I\Omega_s, \\ \mathcal{C}' &\to I'\Lambda' = -I'\Omega_s', \end{aligned} \tag{2.54}$$

where we have identified $\Omega_s = -\Lambda(r = \infty)$ and $\Omega_s' = -\Lambda'(r = \infty)$. Note that when Ω_s is positive (i.e., the spin is in the same direction as the orbital Ω), $\mathcal{C}$ is negative.

A particularly interesting special case is the so-called *irrotational* Darwin-Riemann sequence, for which $\mathcal{C} = \mathcal{C}' = 0$. From equation (2.15), we see that $f_R = f_R{}' = -2$ are also constant along such a sequence. This corresponds to the case where the stars have negligible spin at large r and evolve in the absence viscosity.

In general f_R and $f_R{}'$ vary along the constant-circulation sequences. Numerically, for given $\hat{r}$, eight variables are now required to specify an equilibrium solution: the six variables $\hat{x}_j$ introduced previously plus f_R and $f_R{}'$. Two more functions need to be set equal to zero in the Newton-Raphson scheme (cf. eqs. [2.15] and [2.20]):

$$\begin{aligned} F_7 &= \left(-\frac{1}{5\pi}\kappa_n M\right)\pi a_1 a_2 (2 + f_R)\Omega - \mathcal{C}, \\ F_8 &= \left(-\frac{1}{5\pi}\kappa_n' M'\right)\pi a_1' a_2' (2 + f_R{}')\Omega - \mathcal{C}'. \end{aligned} \tag{2.55}$$

2.3.4 Sequences with Constant Angular Momentum

Since viscous dissipation conserves the total angular momentum, a binary system evolving through viscosity only will follow a sequence of configurations with constant J. Note that, for a

given value of J, the equilibrium sequence is not uniquely determined, since the two stars can have different spins to give the same total angular momentum. However, if initial values of $\mathcal{C}$ and $\mathcal{C}'$ (or f_R and f'_R) are specified, then a unique sequence with $J = $ constant starting from those initial values can be constructed, provided that we know the energy dissipation rate due to viscosity. Constant-J sequences are discussed in more details in §6.2.2.

2.3.5 Asymptotic Solutions for Large r

Explicit solutions of our equations can be obtained analytically in the limit where $r \gg R_o + R'_o$. The results are summarized in Appendix A for several types of equilibrium sequences. These asymptotic solutions for large r have been used in LRS3 to calculate the lowest-order deviations from the point-mass results for the gravitational radiation waveforms emitted during the coalescence of two neutron stars.

3. STABILITY LIMITS AND ROCHE LIMITS

3.1 Secular and Dynamical Stability Limits

In general, stability requires that an equilibrium configuration correspond to a true *minimum* of the total energy $E(\alpha_1, \alpha_2, \ldots; M, J, \ldots)$, i.e., that all eigenvalues of the matrix $(\partial^2 E / \partial \alpha_i \partial \alpha_j)_{eq}$ be positive. The onset of instability along any one-parameter sequence of equilibrium configurations can be determined from the condition (LRS1, §2.3)

$$\det\left(\frac{\partial^2 E}{\partial \alpha_i \partial \alpha_j}\right)_{eq} = 0, \quad i, j = 1, 2, \ldots \quad \text{(onset of instability)}. \quad (3.1)$$

When this condition is satisfied, one of the eigenvalues must change sign. It may then become possible for the system to further minimize its energy by evolving away from the equilibrium configuration considered.

As discussed in LRS1 (§2.4), the nature of the instability depends on the type of perturbation considered about equilibrium. A *dynamical* instability can develop only when J, $\mathcal{C}$ and $\mathcal{C}'$ are all conserved by the perturbation; a *secular* instability requires viscous dissipation, which conserves only J. Mathematically, we locate the point of onset of dynamical instability by evaluating the second derivatives in equation (3.1) holding J, $\mathcal{C}$ and $\mathcal{C}'$ all fixed. If instead we evaluate equation (3.1) by fixing J alone, then we locate the point of onset of secular instability. For general Darwin-Riemann configurations, there are 28 independent matrix elements that need to be evaluated in equation (3.1). They are listed in Appendix B.

Alternatively, we can show that the stability limits determined from equation (3.1) coincide with *turning points* along appropriately constructed equilibrium sequences (LRS1, §2.3). Specifically, a dynamical stability limit coincides with the point where the total equilibrium energy and angular momentum are both minimum along a constant-circulation sequence. A secular stability limit coincides with similar minima appearing along a synchronized sequence. Note that the minima in E and J must coincide along synchronized or constant-circulation sequences since $dE = \Omega \, dJ$ along such sequences (cf. eq. [2.52] and Appendix D of LRS1).

Nonsynchronized configurations can never be true equilibria in the presence of viscosity. Therefore we consider only *dynamical* stability along constant-circulation sequences. A minimum of E and J at some $r = r_m$ along these sequences indicates the onset of dynamical instability. Indeed, at $r = r_m$, it becomes possible for a small dynamical perturbation of the system (which conserves $\mathcal{C}$ and $\mathcal{C}'$) to cause no first-order change in the total equilibrium energy or angular momentum.

This indicates a change of sign in the eigenfrequency ω^2 associated with the perturbation (see, e.g., Shapiro & Teukolsky 1983, Chap. 6).

Along synchronized equilibrium sequences, both secular and dynamical stability limits can exist. A minimum of E and J along these sequences marks the onset of *secular* instability. In the presence of viscosity, configurations with $r < r_m$ will be driven away from synchronization in order to minimize their energy (see §6). The instability at $r = r_m$ cannot be dynamical here because the neighboring configurations along the sequence are still in uniform rotation and cannot be reached by a small perturbation unless viscosity is present. True dynamical instability along a synchronized sequence can occur at some $r < r_m$ where neighboring configurations *with the same values of* $\mathcal{C}$ *and* $\mathcal{C}'$ can be reached with no change in total equilibrium energy to first order. In practice, to obtain the dynamical stability limit along a synchronized sequence parametrized by $\hat{r}$, we can proceed as follows. At every $\hat{r}$, we calculate the equilibrium energy of the synchronized configuration $E_{eq}(\hat{r})$ and the corresponding values of $\mathcal{C}$, $\mathcal{C}'$. We then construct a neighboring equilibrium model, with $\hat{r}$ larger by a small increment $\Delta\hat{r}$, having the same values of $\mathcal{C}$ and $\mathcal{C}'$, and obtain its energy $\tilde{E}_{eq}(\hat{r} + \Delta\hat{r})$. The onset of dynamical instability is then located where $(\tilde{E}_{eq}(\hat{r} + \Delta\hat{r}) - E_{eq}(\hat{r}))/\Delta\hat{r} = 0$.

We can use either the determinant equation (3.1) or the turning point method to locate the critical instability points along an equilibrium sequence. The two methods are mathematically equivalent (cf. LRS1, §2.3). In many cases we have used both criteria to verify the numerical accuracy of our identifications.

To illustrate these points, consider an example where the binary contains two identical components with $n = 0$ (incompressible fluid). We show in Figure 2 how the total equilibrium energy E_{eq} varies along the synchronized sequence, as well as several sequences with constant circulation. The minimum of $E_{eq}(r)$ along the synchronized sequence indicates the onset of secular instability, while the minima along the constant-circulation curves correspond to the onset of dynamical instability. We see that there is a unique point on the synchronized sequence at which the constant-circulation curve that intersects it attains a minimum. This point corresponds to the onset of dynamical instability along the synchronized sequence.

3.2 Roche Limits and Contact Configurations

When the masses of the two binary components are different, a *Roche limit* may exist prior to contact along an equilibrium sequence. Recall that we define contact simply as the point where the surfaces of the two ellipsoids first touch. The Roche limit in our ellipsoidal models is defined as the point where the binary separation r has a minimum value below which no equilibrium solution exists. At the Roche limit, the slope of the $E_{eq}(r)$ curve becomes infinite (cf. Fig. 1). This behavior is somewhat artificial, resulting probably from the truncation of the interaction potential to quadrupole order. The same effect can be seen, but less marked, even in fully numerical solutions going to much higher order but still retaining only a finite number of terms in the multipole expansion of the interaction potential (see §5).

Equilibrium solutions continue to exist beyond the Roche limit (at smaller $\hat{r}$) in some of our models. This second branch of solutions beyond the Roche limit is clearly unphysical since it has higher energy than the main equilibrium branch for the same value of J. The equilibrium configurations beyond the Roche limit must therefore be at least secularly unstable (see §6). Indeed, we note that the Roche limit itself must already be situated beyond the point where E and J are minimum, indicating instability.

Equilibrium sequences for systems with a mass ratio $p = M/M'$ sufficiently close to unity may terminate at $\hat{r} = 1$, i.e., reach contact, before encountering a Roche limit. We do not know if this has any physical significance. Clearly, equilibrium sequences for real systems with $p \neq 1$

14

always terminate at the onset of Roche lobe overflow and mass transfer. This could most naturally be associated with the Roche limit as we define it here. It may be that our contact equilibrium solutions with $p \neq 1$ correspond to true asymmetric contact configurations that can be reached, e.g., after a brief episode of mass transfer in a semidetached system. However, confirmation of this must await more detailed numerical hydrodynamics calculations including the treatment of mass transfer.

3.3 General Classification of the Equilibrium Sequences

Depending on the masses, radii, and polytropic indices of the two components, different behaviors are possible for the equilibrium sequences near contact. We summarize all possible types of behaviors for a synchronized system in Figure 3, where we show schematically the equilibrium energy curves $E_{eq}(r)$, along which we locate the points of secular instability, dynamical instability, and the Roche limit. As discussed above, along such synchronized sequences, the energy minimum corresponds to the onset of secular instability, while the point of minimum r corresponds to the Roche limit.

Six different possible behaviors can be distinguished:

(a) The binary encounters no stability or Roche limit prior to contact, hence stable equilibrium solutions exist all the way to contact.

(b) The binary encounters a secular stability limit prior to contact, but no dynamical stability or Roche limit. Beyond the secular stability limit, the system becomes unstable on the viscous dissipation time scale, but all equilibrium solutions are dynamically stable.

(c) The binary encounters a secular stability limit and a Roche limit before contact, but not a dynamical stability limit. The binary at the Roche limit is secularly unstable but dynamically stable.

(d) The binary encounters a secular stability limit and a dynamical stability limit prior to contact, but not a Roche limit. The system becomes secularly unstable first, then dynamically unstable.

(e) The binary encounters a secular stability limit, a dynamical stability limit and a Roche limit prior to contact. The binary becomes dynamically unstable before the Roche limit is reached, and thus a binary at the Roche limit is dynamically unstable.

(f) The binary encounters a secular stability limit, a Roche limit and a dynamical stability limit prior to contact. The Roche limit is reached prior to the dynamical stability limit. The binary at the Roche limit is secularly unstable but dynamically stable.

The situation for equilibrium sequences with constant circulation is simpler. In this case, the minimum of $E_{eq}(r)$ corresponds to the dynamical stability limit. The different behaviors can then be summarized as (a)-(c) in Fig. 3. For (a), equilibrium solutions all the way to contact are dynamically stable; for (b) a dynamical instability is encountered prior to contact; for (c) the binary first encounters a dynamical stability limit and then a Roche limit prior to contact.

4. APPLICATIONS

In this section, we show how the general Darwin-Riemann configurations for polytropes can be used to construct simple models for a variety of different astrophysical systems. We exploit the freedom to assign different polytropic indices n and n' and different constants K and K' for the two components. The choice of n and n' allows us to model the distribution of mass inside each component independently, while the choice of K and K' allows us to mimic different types of realistic mass-radius relations (cf. eq. [2.39]).

4.1 Models with $K = K'$: Low-mass White Dwarfs and Planets

Low-mass white dwarfs with $10^{-3} \ll M/M_\odot \ll 1$ are supported by degenerate pressure from nonrelativistic ideal electrons (see, e.g., Shapiro & Teukolsky 1983). In this mass range, the equation of state is that of a polytrope with $n = 1.5$ and $K = 1.0036 \times 10^{13}/\mu_e^{5/3}$ (cgs), where $\mu_e = \langle A/Z \rangle$ is the mean molecular weight per electron, A is the atomic weight and Z is the atomic number; both n and K are independent of mass. Thus for a binary consisting of two white dwarfs with masses M and M' in this range, the ratio of the stellar radii is $R_o/R'_o = (M/M')^{(1-n)/(3-n)} = (M/M')^{-1/3}$.

Models with $K = K'$ can also be applied crudely to cold objects with sufficiently low mass, $M \ll 10^{-3}M_\odot$ (Zapolsky & Salpeter 1969; Lai, Abrahams & Shapiro 1991), such as planets and their satellites. For these objects, solid state (Coulomb) forces render the equation of state quite stiff and the density nearly uniform, i.e., the configurations are nearly incompressible with $n \simeq 0$. Thus for binary systems containing these objects, we can take $R_o/R'_o = (M/M')^{1/3}$.

Some equilibrium properties for systems with $K = K'$ were shown in Figure 1. The systems are assumed to be synchronized ($f_R = f'_R = 0$), and have $n = n' = 1.5$. Different curves correspond to different mass ratios: $p = 1, 0.8, 0.6$, and 0.5. All sequences terminate at contact, where $\hat{r} = 1$. We see that for $n = 1.5$, all sequences encounter a secular stability limit (minimum of E and J) prior to contact. When M and M' are sufficiently different, a Roche limit is found prior to contact.

In Table 1 we present selected equilibrium sequences for synchronized Darwin-Riemann binaries with $K = K'$ and $n = n'$. Each sequence is parametrized by monotonically decreasing values of the parameter $\hat{r}$ (cf. eq. [2.50]). All sequences terminate at contact ($\hat{r} = 1$) or at the Roche limit. For each equilibrium solution, we list various physical properties of interest, including the ratios a_2/a_1, a_3/a_1, R/R_o, and the quantities

$$\bar{r} = \frac{r}{R_o + R'_o}, \quad \bar{\Omega} = \frac{\Omega}{(\pi G \bar{\rho}_o)^{1/2}}, \quad \bar{J} = \frac{J}{(GM^3 R_o)^{1/2}}, \quad \bar{E} = \frac{E}{(GM^2/R_o)}, \quad (4.1)$$

where $\bar{\rho}_o \equiv M/(4\pi R_o^3/3)$.

The three critical points, i.e., the secular stability limit r_{sec}, the dynamical stability limit r_{dyn} and the Roche limit r_{lim}, along an equilibrium sequence can be calculated using the method discussed in §3. In Table 2 we give some results for the synchronized configurations ($f_R = f'_R = 0$) with $n = n' = 0, 0.5, 1.5, 2.5$. Several different values of $p = M/M'$ are considered for each n. At each of these critical points, various physical quantities are given. Note that for given n and p, not all of these critical points exist prior to contact. When they do exist, we list them in the order of decreasing $\hat{r}$. As noted before, along an equilibrium sequence, $\hat{r}$ monotonically decreases, whereas $\bar{r}$ can increase beyond the Roche limit. Therefore the critical point with larger $\hat{r}$ occurs prior to that with smaller $\hat{r}$. The existence of these critical points and the order of their appearance (cf. Fig. 3) depend on the values of n and p.

Consider the two interesting cases with $n = 0$ and $n = 1.5$. For the n=0 case, both the secular and dynamical stability limits always exist. When $p < 0.79$, a Roche limit also appears. The dynamical stability limit appears prior to the Roche limit, except when $p < 0.0042$, for which a Roche-Riemann model is well adequate to describe the binary (see below). Now consider the $n = 1.5$ case. For $p = 1$, only a secular stability limit exists prior to contact. As the mass ratio decreases to $p < 0.76$, a dynamical instability arises; when $p < 0.745$, a Roche limit also appears. For $0.267 < p < 0.745$, the dynamical instability is encountered prior to the Roche limit; but for $p < 0.267$, the Roche limit is encountered first.

To summarize, we show in Figure 4 (i) a $p - n$ diagram, distinguishing the different behaviors illustrated in Figure 3. The figure treats synchronized configurations only. The diagram was

constructed as follows. For given n and p, we first determine whether a critical point exists prior to contact. For this we only need to solve for two neighboring equilibrium configurations around $\hat{r} = 1$, and compare the values of $\bar{r}$, E_{eq} (or J_{eq}) for these two neighboring solutions (cf. §3 and Fig. 3). For example, if $\Delta\bar{r}/\Delta\hat{r} > 0$ at $\hat{r} = 1$, then a Roche limit does not occur prior to contact; otherwise a Roche limit exists. When the dynamical stability limit and the Roche limit both exist, we need to determine which one occurs first by comparing the values of $\hat{r}$ at which they occur. In Figure 4 (i), only the boundary line between regions (e) and (f) requires solving for the values of $\hat{r}_{dyn}$ and $\hat{r}_{lim}$. From Figure 4 (i), we see that for the binaries to be dynamically stable at the Roche limit, the stars must be sufficiently compressible (large n), or the masses of the two components must be significantly different. Moreover, as $n \to 3$, a Roche limit always occurs before contact.

A similar diagram for irrotational configurations with $K = K'$ is shown in Figure 5 (i). Here the Roche limit configuration, if exists at all, is always dynamically unstable.

When $K = K'$, the less massive companion always suffers a larger tidal deformation. This can be seen from Table 1 by comparing the axis ratios of the two components (e.g., a_2/a_1 vs. a_2'/a_1'). When $p = M/M'$ is sufficiently small, the more massive star suffers little tidal deformation and can be treated as a point mass. The binary can then be modeled as a Roche-Riemann configuration (see §4.4).

4.2 Models with $R_o/R_o' = M/M'$: Low-mass Main-Sequence Stars

Low-mass main-sequence (MS) stars with $0.1 M_\odot \lesssim M \lesssim 0.8 M_\odot$ have extensive convective envelopes and can be modeled approximately as polytropes with $n \simeq 1.5$–3. For reference, we have constructed polytropic models of low-mass, Pop II MS stars by simply matching the radius and ratio of central to mean density obtained in detailed stellar structure calculations (D'Antona 1987). In Table 3 we list the radii and effective n obtained for different masses. The mass-radius relation can be fitted approximately by a power-law relation $R_o \propto M^\alpha$, with $\alpha \simeq 0.8$–1. Here, for simplicity, we adopt $\alpha = 1$ and we model the stars as polytropes with $n = n'$, and with K and K' adjusted to obtain $R_o/R_o' = M/M'$. We assume synchronization, since the effective viscosity in convective envelopes is very large (Zahn 1977).

In Figure 4 (ii), we show the $p - n$ diagram distinguishing the different types of equilibrium sequences for this model. In particular for $n = 1.5$, we find that secular instability always sets in prior to contact or the Roche limit. When $p < 0.56$, dynamical instability can also arise. These results are only partially confirmed by more accurate, fully numerical calculations, which indicate that Roche lobe overflow occurs before any instability when the mass ratio p is sufficiently close to unity (see §5). Dynamical instabilities in models with $n = n' = 1.5$ have been identified in fully numerical solutions, but only for equilibrium configurations where the two stars are in deep contact (see Rasio 1993; Rasio & Shapiro 1993).

4.3 Models with $R_o = R_o'$: Neutron Stars and Brown Dwarfs

The internal structure of neutron stars is determined by the nuclear equation of state (EOS) (see, e.g., Shapiro & Teukolsky 1983). They are generally characterized by a very stiff polytropic index $n \simeq 0.5$–1 for masses well above the minimum mass ($M \gtrsim 0.1 M_\odot$). For many realistic EOS, the stellar radius is not very sensitive to the mass for an appreciable mass range. For example, the recent nuclear EOS of Wiringa, Fiks & Fabrocini (1988) gives a value of $R_o \simeq 10\,\mathrm{km}$ almost independent of the mass for $0.8 M_\odot \lesssim M \lesssim 1.5 M_\odot$. Thus for a simple description of binary neutron stars we can adopt $R_o/R_o' = 1$ and $n = n' \simeq 0.5$–1.

For brown dwarfs with $0.001 \lesssim M/M_\odot \lesssim 0.08$, the dependence of radius on mass is also very weak (Zapolsky & Salpeter 1969; Lai et al. 1991; Burrows & Liebert 1993). Therefore models with $R_o/R_o' = 1$ can also be used to describe approximately brown dwarf binaries, although here

17

$n \lesssim 1.5$.

Figure 4 (iii) shows the $p - n$ diagram for synchronized configurations with $R_o/R_o' = 1$ and $n = n'$. The similarity with Figure 4 (i) is expected, since here also the more massive star suffers less tidal deformation (see §4.5). Figure 5 (ii) shows the analogous diagram for irrotational configurations.

The evolution of most close binary systems that are observed may be tracked along sequences of synchronized equilibrium configurations. But this may not be true for neutron star binaries undergoing orbital decay due to gravitational radiation emission Bildsten & Cutler 1992; Kochanek 1992). In this case, the viscous dissipation time may never be small enough to achieve synchronization. Therefore binary neutron stars may actually evolve along irrotational equilibrium sequences (Kochanek 1992). We see from Figure 5 (ii) that all irrotational sequences contain a dynamical stability limit as long as $n \lesssim 1.2$. Thus all neutrons star binaries (except those containing very low-mass components) encounter a dynamical instability during their evolution. In particular, for typical $n = 0.5$–1, we see that the Roche limit configuration is always dynamically unstable. On the basis of this result (confirmed by recent fully numerical calculations; see Rasio & Shapiro 1993), we argued in LRS3 that stable mass transfer in binary neutron stars (as proposed by Clark & Eardley 1977; see also Jaranowski & Krolak 1992) cannot occur. The only exception would be when the mass of one of the two components is very small ($M \lesssim 0.4 M_\odot$) and the viscosity is sufficient to maintain synchronization. Indeed, we see in Figure 4 (iii) that dynamically stable Roche limit configurations can exist for synchronized systems only when $n \gtrsim 1.5$, or when the mass ratio p is very small.

The irrotational sequences correspond to neutron stars with no intrinsic spin (see eq. [2.54]). When the stars have nonzero spins, the appropriate sequences are those with constant $\mathcal{C}$ and $\mathcal{C}'$ (§2.3.3). Examples of such sequences are tabulated in LRS3, where a more realistic model for neutron stars has also been considered. In this more realistic model, the radius and effective polytropic index are obtained from the nuclear EOS of Wiringa et al. (1988).

4.4 Extreme Mass Ratios: Roche-Riemann Binaries

Let us compare the tidal deformation of the two components in a general Darwin-Riemann configuration. The ellipticity of M due to the tidal field of M' can be estimated as

$$\varepsilon \sim \frac{\Delta R}{R} \sim \frac{M'}{M} \left(\frac{R_o}{r} \right)^3. \tag{4.2}$$

Similarly for M',

$$\varepsilon' \sim \frac{M}{M'} \left(\frac{R_o'}{r} \right)^3. \tag{4.3}$$

Clearly we have

$$\varepsilon' \sim \varepsilon \left(\frac{M}{M'} \right)^2 \left(\frac{R_o'}{R_o} \right)^3 = \varepsilon \left(\frac{M}{M'} \right)^{2-3\alpha} = \varepsilon p^{2-3\alpha}, \tag{4.4}$$

where we have assumed that $R_o/R_o' = (M/M')^\alpha$. We see that when $\alpha < 2/3$, $\varepsilon' \to 0$ as the mass ratio $p = M/M' \to 0$, i.e., the more massive star suffers no tidal deformation and behaves like a point mass in this limit. Therefore when $\alpha < 2/3$, our Darwin-Riemann solutions should approach the Roche-Riemann solutions (LRS1, §8) for sufficiently small p (and as long as spin effects can be neglected). This is confirmed by our numerical calculations.

Consider first the models with $K = K'$ and $n = n'$ (§4.1). For these models we have $\alpha = (1 - n)/(3 - n)$, so the inequality $\alpha < 2/3$ is always satisfied. Thus for small p, these models

become Roche-Riemann configuration. For example, in the model of a planet-satellite system, we can take $n = 0$ so that $\alpha = 1/3$, and we have $M_{planet} \gg M_{satellite}$, so that the tidal deformation of the planet is negligible. The planet can therefore be represented by a point mass, even though its size is much larger than that of the satellite. The binary neutron star models with $R_o = R'_o$ discussed in §4.3 also have this asymptotic property.

In contrast, for typical low-mass MS stars with $0.8 \lesssim \alpha \lesssim 1$ (§4.2), we have the opposite result: the more massive star suffers a larger tidal deformation than the less massive star as a result of its much larger size. In fact, in this case, as $p \to 0$, we approach the extreme opposite limit of a Roche-Riemann configuration, i.e., a test particle around a massive companion (see LRS1, §8.3).

As discussed in LRS1, irrotational Roche-Riemann configurations always encounter a dynamical stability limit (minimum of E and J) followed by a Roche limit (minimum of r), while the synchronized Roche configurations always encounter a secular stability limit followed by a Roche limit. The existence of a dynamical instability for Roche configurations depends on the values of p and n. We show in Figure 6 the boundary line between the two regimes. As expected, this line coincides exactly with the long-dashed lines in Figure 4 (i) and (iii) in the limit of small p. Note that for $p = 0$ (e.g., a star orbiting synchronously around a supermassive black hole), the Roche limit is always encountered prior to the dynamical stability limit.

5. COMPARISON WITH RECENT NUMERICAL WORK

To assess the validity of our binary equilibrium models, we have performed extensive comparisons with the results of fully numerical studies by Hachisu and Eriguchi (1984b, herafter HE), who used a grid-based technique in three dimensions, as well as our own recent calculations using the smoothed particle hydrodynamics (SPH) method (see Monaghan 1993 for a recent review). The SPH method is used to construct hydrostatic equilibrium configurations by letting a system containing initially two spherical polytropes relax in the presence of artificial friction forces. The binary separation r is maintained constant during the calculation, which is performed in the corotating frame of the binary. See Rasio & Shapiro (1992, 1993) for details. Similar comparisons were presented in LRS1 for binary models containing two identical components. Here we present selected results for binary models with mass ratio $p \neq 1$. The comparison is limited to synchronized models (Darwin configurations) since no numerical data are available for nonsynchronized configurations in three dimensions. While the self-consistent-field method of HE can only give hydrostatic equilibrium solutions, the SPH method can be used to test directly the dynamical stability of the solutions. This is done simply by using the equilibrium configuration as an initial condition for a dynamical calculation. Unstable systems evolve to a rapid coalescence and merging of the two components in just a few orbital periods, while stable systems maintain their circular orbit indefinitely (Rasio & Shapiro 1992, 1993).

In Figure 7 we compare our ellipsoidal results for incompressible Darwin models ($n = n' = 0$, $f_R = f'_R = 0$) with $p = 1.5$, 5, and 10, to those of HE. Following HE here for convenience, we show the variation of Ω^2 as a function of J, and we adopt the units defined in equations (4.1) (note that $R = R_o$ in the incompressible case). We note immediately that *both calculations agree in predicting the existence of a minimum of J prior to the Roche limit*. This is an important point, which gives us complete confidence that the secular instability identified here is real and not a mathematical artefact caused by our simplifying approximations. Indeed, HE interpret correctly the existence of the minimum in terms of a secular instability, which they refer to as the "gravogyro" instability. Quantitatively, the agreement between our results and those of HE is excellent away from the Roche limit. Very near the Roche limit, the truncation of the interaction potential to quadrupole order introduces nonnegligible errors in our models. As a result, the Roche limit appears slightly earlier along the numerically determined sequence. As expected, the deviations are smaller for

19

systems with more extreme mass ratios where the Roche limit is at larger r. Note that the Roche limit also appears as a turning point (where $d\Omega^2/dJ = 0$) followed by a (very short) second branch of equilibrium solutions in the calculations of HE. As discussed in §3.2, we believe this to be the result of truncating the interaction potential to some high but finite order in a multipole expansion. Unfortunately, the numerical calculations of HE were limited to the incompressible case (Hachisu & Eriguchi 1984a and Hachisu 1986b have considered compressible binary models, but only with $p = 1$). Rasio & Shapiro (1993) have recently performed a series of calculations for compressible systems with $p \neq 1$ using the SPH method. As far as we are aware, these are the first three-dimensional calculations for compressible binary systems with $M \neq M'$.

In Figure 8 we present a comparison with these recent SPH results for models of main-sequence star binaries with $n = n' = 1.5$ and $R_o/R'_o = M/M'$ (cf. §4.2). For $p = 1$ it is possible to extend the equilibrium sequence calculated with SPH all the way into deep contact. This sequence (Fig. 8a) terminates when mass shedding occurs through the outer Lagrangian points. In contrast, all sequences with $p = M/M' \neq 1$ terminate at the onset of Roche lobe overflow, beyond which an equilibrium solution no longer exists for that value of p. In all cases, the equilibrium $J(r)$ curves determined by the two methods are in excellent quantitative agreement all the way to the onset of Roche lobe overflow or point of first contact (for $p = 1$), as determined by SPH. An important conclusion is that, *for sufficiently compressible fluids*, the much simpler quasi-analytic results derived here can be used even for applications requiring high quantitative accuracy, as long as the precise location of the Roche limit is not required. A similar situation was encountered in LRS1 (cf. §3 of that paper) with respect to the mass shedding limit along equilibrium sequences of single rotating stars. The energy variational method can be used to determine equilibrium properties of uniformly rotating polytropes quite accurately up to the mass shedding limit, but it cannot by itself predict accurately the position of the mass shedding limit. Note also in Figure 8 that the numerically determined terminal configurations, corresponding to the onset of Roche lobe overflow and mass transfer, are secularly unstable (past the minimum of J) only for sufficiently small mass ratios ($p \lesssim 0.5$). This is in contrast with the prediction of §4.2, that all Roche limit configurations should be secularly unstable in this case. In addition, all SPH solutions with $0.25 \leq p < 1$ remain dynamically stable all the way to the Roche limit. The sequence of contact solutions with $p = 1$ (beyond the point marked C in Fig. 8a) encounters a dynamical instability prior to the mass shedding limit (onset of mass loss through the outer Lagrangian points; see Rasio & Shapiro 1993 for details).

In Figure 9, we show a similar comparison with SPH for models of a binary containing two highly-incompressible degenerate stars with $n = n' = 0.5$, $K = K'$, and $p = 0.85$. *The two methods agree in predicting that the Roche limit configuration is both secularly and dynamically unstable*. Quantitatively, the agreement is excellent prior to the minimum of J (deviations are $\ll 1\%$ between the two $J(r)$ curves), and slightly less good ($\sim 1\%$) from the minimum of J to the Roche limit. The values of r_{sec}/R_o predicted by the two methods agree to within 5%, the values of r_{lim}/R_o within 10%. We conclude that, *for sufficiently incompressible fluids*, the quantitative accuracy of the ellipsoidal solutions is always excellent, both for determining the global physical properties along an equilibrium sequence and for locating the onset of instability and Roche lobe overflow.

6. BINARY EVOLUTION TRACKS

In this section, we show how the equilibrium sequences calculated in §4 can be used to describe the secular orbital evolution of close binary systems in the presence of dissipation. We consider two astrophysically important dissipation mechanisms that can drive orbital evolution: viscosity and gravitational radiation. We first derive the secular rates of dissipation due to these mechanisms for binaries in circular orbit. Our treatment is exact in the ellipsoidal approximation.

20

6.1 Dissipation Rates and Time Scales

6.1.1 Viscous Dissipation

In any fluid system, the rate of energy loss due to shear viscosity is given by (Landau & Lifshitz 1987)

$$\dot{E}_v = -\int \sigma_{ij} v_{i,j} \, d^3x, \tag{6.1}$$

where v_i is the fluid velocity and σ_{ij} is the viscous stress tensor,

$$\sigma_{ij} = \eta \left(v_{i,j} + v_{j,i} - \frac{2}{3} \delta_{ij} v_{k,k} \right). \tag{6.2}$$

We denote by $\eta = \rho\nu$ the dynamical shear viscosity, where ν is the kinematic shear viscosity (units cm^2/s). Consider the viscous dissipation in the star of mass M. Using equation (2.14) with $\mathbf{u}^{(0)} = \mathbf{v}$ here, we get

$$\begin{aligned} v_{1,2} &= \frac{a_1}{a_2}\Lambda - \Omega, \\ v_{2,1} &= -\frac{a_2}{a_1}\Lambda + \Omega, \\ v_{i,j} &= 0 \quad \text{otherwise.} \end{aligned} \tag{6.3}$$

Thus the rate of viscous energy dissipation is given by

$$\dot{E}_v(M) = -\bar{\nu} M \Lambda^2 \left(\frac{a_1^2 - a_2^2}{a_1 a_2} \right)^2, \tag{6.4}$$

where $\bar{\nu} = \frac{1}{M} \int \nu \, dm$ is the mass-averaged viscosity. The viscous dissipation rate $\dot{E}_v(M')$ in the star of mass M' can be written down similarly. We see that $\dot{E}_v(M) \propto \Lambda^2$, so that the viscous dissipation vanishes for synchronized configurations, as expected.

Since viscous forces conserve the total angular momentum, we have $\dot{J}_v = 0$. From equation (2.52), we then obtain the secular rate of change of circulation in M,

$$\dot{\mathcal{C}}_v(M) = \frac{\dot{E}_v(M)}{\Lambda} = -\bar{\nu} M \Lambda \left(\frac{a_1^2 - a_2^2}{a_1 a_2} \right)^2, \tag{6.5}$$

and a similar expression for M'.

6.1.2 Gravitational Radiation

In the weak-field, slow-motion limit of general relativity, the total rate of energy loss due to gravitational wave emission is given by (cf. LRS3)

$$\dot{E}_{GW} = -\frac{32G}{5c^5} \Omega^6 (\mu r^2)^2 \left[1 + \frac{1}{\mu r^2}(I_{11} + I'_{11} - I_{22} - I'_{22}) \right]^2. \tag{6.6}$$

This is essentially the quadrupole formula (see, e.g., Shapiro & Teukolsky, Chap. 16) written for a binary system containing two ellipsoids. Fluid circulation is conserved by the gravitational

radiation reaction forces, i.e., $\dot{\mathcal{C}}_{GW} = \dot{\mathcal{C}}'_{GW} = 0$ (Miller 1974). From equation (2.52), the secular rate of angular momentum loss is given by

$$\dot{J}_{GW} = \frac{\dot{E}_{GW}}{\Omega}. \tag{6.7}$$

Other energy and angular momentum loss mechanisms such as magnetic braking and mass loss from the system are far more difficult to model and will not be considered here. However, we expect our qualitative discussion below to hold quite generally.

6.1.3 Time Scales

There are four physically distinct time scales relevant to the evolution of the binaries: the internal hydrodynamical time, $t_{dyn} \equiv (R_o^3/GM)^{1/2}$; the orbital period, $P = 2\pi/\Omega$; the time scale for the fluid circulation to change, $t_{\mathcal{C}} \equiv |\mathcal{C}/\dot{\mathcal{C}}|$; the time scale for angular momentum loss, $t_J \equiv |J/\dot{J}|$. Most binary systems have $t_{dyn} < P < t_{\mathcal{C}} < t_J$.

For angular momentum loss due to gravitational wave emission, t_J is given by (cf. eqs. [6.6] and [6.7])

$$t_J = \frac{5c^5}{64G^3} \frac{r^4}{MM'(M + M')}. \tag{6.8}$$

To estimate $t_{\mathcal{C}}$, we use equations (2.20) and (2.54) to write $\Lambda \simeq \Omega - \Omega_s$ for large r. The angular frequency Λ thus measures the departure from synchronization. From equation (6.5) we then get

$$t_{\mathcal{C}} \simeq \left(\frac{a_1 a_2}{a_1^2 - a_2^2} \right)^2 \left(\frac{R_o^2}{\bar{\nu}} \right) \frac{\Omega_s}{\Lambda}. \tag{6.9}$$

Note that $t_{\mathcal{C}}$ is propotional to the viscous dissipation time $t_{vis} \equiv R_o^2/\bar{\nu}$. Note also that exact synchronization can never be achieved, since $t_{\mathcal{C}} \to \infty$ as $\Lambda \to 0$.

Using $a_1 \sim a_2 \sim R_o$ and $(a_1 - a_2)/R_o \sim (M'/M)(R_o/r)^3$, equation (6.9) gives

$$t_{\mathcal{C}} \sim \frac{\Omega_s}{\Lambda} t_{syn} \tag{6.10}$$

where we have defined the synchronization time

$$t_{syn} \equiv \left(\frac{M}{M'} \right)^2 \left(\frac{r}{R_o} \right)^6 \frac{(GMR_o)^{1/2}}{\bar{\nu}} \left(\frac{R_o^3}{GM} \right)^{1/2}. \tag{6.11}$$

This scaling for t_{syn} agrees with the results of the standard weak-friction model of tidal interactions (Alexander 1973; Zahn 1977). For solar-type MS stars, the average plasma viscosity is of order 10^3 cm^2/s, corresponding to $\bar{\nu}/(GMR_o)^{1/2} \sim 10^{-15}$. This is far too small to explain the high degree of synchronization observed in close MS star binaries. However, turbulent viscosity associated with convection in late-type systems can give $1 \gtrsim \bar{\nu}/(GMR_o)^{1/2} \gg 10^{-15}$ (Zahn 1977). Possible sources of anomalous viscosity in degenerate stars are discussed by Kochanek (1992).

6.2 Orbital Evolution

6.2.1 Basic Assumptions

Depending on which mechanism dominates, the time scale for energy loss according to equation (2.52) can be either t_J or $t_{\mathcal{C}}$, i.e., $t_E \equiv |E/\dot{E}| \sim \min(t_{\mathcal{C}}, t_J)$. We only consider regimes where

both t_J and t_C are much longer than P and t_{dyn}, so that the binary evolves quasi-statically along an equilibrium sequence. This applies to the majority of observed binary systems, with the possible exception of neutron star binaries near coalescence. The secular rate of change of the binary separation can then be written

$$\dot{r} = \frac{\dot{E}}{dE_{eq}/dr},\qquad(6.12)$$

and the orbital evolution time t_r is given by

$$t_r \equiv \frac{r}{|\dot{r}|} = \frac{r|dE_{eq}/dr|}{|\dot{E}|}.\qquad(6.13)$$

Normally, when $|dE_{eq}/dr| \sim |E/r|$, we have $t_r \sim t_E$, i.e., the orbit decays on the energy loss time scale. But it is important to note that t_r can become significantly smaller than t_E as $dE_{eq}/dr \to 0$. The quasi-static description of the orbital evolution becomes invalid when a dynamical stability is approached.

There are two regimes of interest. When the fluid viscosity is sufficiently small so that $t_{syn} \gg t_J$, the evolution of a binary system as it loses angular momentum proceeds along constant-circulation equilibrium curves such as those shown in Figure 3. The values of $\mathcal{C}$ and $\mathcal{C}'$ are determined by the initial spins of the stars (cf. eqs. [2.54]). The orbit decays on the time scale $t_E \sim t_J$ until a dynamical instability is encountered, followed by rapid coalescence and merging of the two stars (Rasio & Shapiro 1992, 1993). This regime is most relevant to the coalescence of binary neutron stars driven by gravitational radiation. Indeed, for these systems, it has been argued that the viscosity is always too small to maintain synchronization (Bildsten & Cutler 1992; Kochanek 1992). We refer the reader to our discussion of this regime in LRS3 for more details.

Here we focus on the opposite regime when viscosity dominates and $t_{syn} \ll t_J$. This regime applies to most observed binary systems containing at least one nondegenerate component. The inequality can be written

$$\frac{t_{syn}}{t_J} \sim \left(\frac{r}{R_o}\right)^2 \left(\frac{GM}{c^2 R_o}\right)^{5/2} \frac{(GMR_o)^{1/2}}{\bar{\nu}} \ll 1.\qquad(6.14)$$

In this regime, binaries evolve along constant$-J$ equilibrium sequences. In general, for a fixed value of J, the equilibrium sequence is not unique: even at large separation, fixing J and r determines only the sum of the two spin angular momenta. However, if a complete initial configuration is specified with given values of $\mathcal{C}$ and $\mathcal{C}'$ (or f_R and f'_R), then the constant$-J$ sequence passing through the initial configuration can be constructed uniquely provided we know the ratio of the averaged viscosities within the two components.

6.2.2 Evolution along Constant-J Sequences

For simplicity, we treat only the case where the binary contains two identical components. In Figure 10 we show examples of constant$-J$ equilibrium curves for $n = 1.5$ and $p = 1$. Three values of J are considered. We also show the synchronized (Darwin) sequence for comparison. We see that there exists a critical value $J = J_{min}$, equal to the minimum of J along the synchronized sequence, above which a constant$-J$ sequence intersects the synchronized sequence. Moreover, this intersection point exactly coincides with an energy extremum along the constant$-J$ sequence. This is easy to understand: from equation (2.52) we have $dE = 2\Lambda\, d\mathcal{C}$ along a constant$-J$ sequence; thus when $\Lambda = 0$ (at synchronization), $dE = 0$. For the case shown in Figure 10, the intersection point (point B in Fig. 10a) lies on the secularly stable branch of the synchronized sequence. Therefore,

it is the point of minimum energy along the corresponding constant$-J$ sequence, i.e., among all those configurations with the same J, the synchronized configuration is the one that has the lowest energy.

Note that if we consider a value of J just slightly greater than J_{min}, the constant$-J$ curve can intersect the synchronized curve twice, once on the secularly stable branch and once on the unstable branch (Fig. 10b). Both intersection points correspond to a local energy extremum along the constant-J sequence. The intersection with the stable branch is a minimum (point H in Fig. 10b), whereas the intersection with the unstable branch is a maximum (point I in Fig. 10b). This explains very clearly the physical nature of the secular instability. Viscosity will drive a secularly unstable equilibrium configuration *away* from synchronization at first. As a result, the orbit can either expand (along IH) as the system is driven towards a lower-energy, stable synchronized state, or it can decay (along IJ) as the stars are driven to coalescence.

For the limiting case where $J = J_{min}$, the constant$-J$ sequence passes through the secular stability limit point along the synchronized sequence (point C in Fig. 10a). In this case, the intersection is a stationary point ($dE_{eq}/dr = 0$, $d^2E_{eq}/dr^2 = 0$) of the $E_{eq}(r)$ curve for the the constant$-J$ sequence. Note that the first secularly unstable synchronized configuration at point C will always be driven to coalescence by viscous dissipation (in contrast to unstable configurations beyond C, for which the orbit can evolve either way). When $J < J_{min}$, the constant$-J$ sequence never intersects the synchronized sequence, and the energy decreases monotonically as r decreases. Therefore, configurations with $J < J_{min}$ can never reach synchronization, and are always driven to coalescence by viscous dissipation.

Clearly, the orbital evolution of a binary system depends critically on its initial angular momentum J_i. When $J_i < J_{min}$, as the the binary losses energy due to viscous dissipation, it simply slides down the constant$-J$ curve (e.g., along FG in Fig. 10a). The time scale for this orbital decay is the synchronization time, since $t_r \sim t_\mathcal{C} \sim t_{syn}$ in this case. When $J_i > J_{min}$, the binary first evolves toward a (stable) synchronized configuration. If the star initially spins faster than the synchronized rate (point E in Fig. 10a), the orbit expands as the system evolves toward synchronization (along EB). The Earth-Moon system is a well-known example of such an evolution. If the initial spin is slower than the synchronized rate (point A), then the separation becomes smaller as the binary evolves toward synchronization (along AB). This evolution takes place on a time scale $t_r \sim t_\mathcal{C}$. Initially $t_\mathcal{C} \sim t_{syn}$; but $t_\mathcal{C}$ increases as synchronization is approached (cf. eq. [6.9]). As viscous energy dissipation falls asymptotically to zero ($\dot{E}_v \propto \Lambda^2$), the orbit will cease to evolve if there is no other dissipation mechanism.

6.2.3 Final Approach to Instability

Now consider what happens to a nearly synchronized system if it is losing angular momentum by some additional process like gravitational radiation. As the orbit decays, the binary will very closely track the synchronized curve (along BC in Fig. 10a) with $\Omega \simeq \Omega_s$ and evolve toward a lower energy and angular momentum state. This evolution takes place on the angular momentum loss time scale, with of $t_r \sim t_J \gg t_{syn}$. The degree of synchronization can be estimated by setting $t_r \sim t_J \sim t_\mathcal{C}$, which yields $\Lambda/\Omega \sim t_{syn}/t_J \ll 1$. Viscous dissipation is negligible during this phase, as $\dot{E}_v \sim \mathcal{C}\Lambda/t_\mathcal{C} \sim I\Omega\Lambda/t_J \sim \dot{E}_{GW}(\Lambda/\Omega)$. Equation (6.12) applies, with $E_{eq}(r)$ calculated for the synchronized sequence (§2.3.2) and $\dot{E} = \dot{E}_{GW}$ (eq. [6.6]).

As the binary approaches the energy minimum (i.e., the secular stability limit, at point C), the orbital decay time t_r become shorter and shorter as $dE_{eq}/dr \to 0$ (cf. eq. [6.13]). At some point prior to the energy minimum, t_r becomes comparable to t_{syn}, i.e., the orbit decays so fast that viscosity can no longer maintain synchronization. Clearly, the evolution cannot follow the synchronized sequence beyond the point of energy minimum. As Λ becomes comparable to Ω, vis-

24

cous dissipation resumes and eventually becomes dominant, with $\dot{E}_v \gg \dot{E}_{GW}$. Note that viscosity is now driving the system *away from synchronization*. The subsequent and final evolution follows closely the constant-J curve with $J = J_{min}$ (along CD in Fig. 10a). Thus the final coalescence takes place on a time scale $t_r \sim t_{\mathcal{C}} \sim t_{syn} \ll t_J$. It is driven almost entirely by internal viscous dissipation, with angular momentum loss playing a negligible role.

The terminal phase of the orbital decay outlined above requires modification when a dynamical stability limit exists. Consider the binary sequences with $p = 1$ and $n = 0$ shown in Figure 11. We consider again three constant-J sequences with $J > J_{min}$, $J = J_{min}$ and $J < J_{min}$, where J_{min} is the minimum angular momentum along the synchronized sequence. A dynamical stability limit is encountered prior to contact for all these sequences. Along a constant-J sequence, the dynamical stability limit corresponds to an extremum in both energy and circulation $\mathcal{C}$, as $dE = 2\Lambda\, d\mathcal{C} = 0$. This is analogous to the dynamical stability limit along a constant$-\mathcal{C}$ sequence, where $dE = dJ = 0$. As in Figure 10, for $J > J_{min}$, the constant-J curves also intersect the synchronized sequence where they reach an energy extremum (as $dE = 2\Lambda d\mathcal{C}$ with $\Lambda = 0$). Therefore, there are now *three* extrema along a constant-J sequence with $J > J_{min}$.

Now consider the orbital evolution of the systems shown in Figure 11. When $J > J_{min}$, viscosity first drives the binary to a synchronized state in a time $\sim t_{syn}$ (along EB or AB, depending on whether the initial spin rate is larger or smaller than the synchronized spin rate). Then the binary follows closely the synchronized sequence (along BC) for a time $\sim t_J$, until the secular stability limit is reached (point C). Beyond that point the evolution follows the constant $J = J_{min}$ sequence (along CD), for a time $\sim t_{\mathcal{C}} \sim t_{syn}$. Before reaching contact, however, the system becomes dynamically unstable (point D), and equation (6.12) is no longer valid. The coalescence accelerates abruptly and the two stars merge in a time $\sim P$. This transition to a dynamical coalescence has been studied in LRS2 and LRS3. Similarly, when $J < J_{min}$, the binary slides down the constant$-J$ curve (along HI) in a time $\sim t_{\mathcal{C}} \sim t_{syn}$ and eventually becomes dynamically unstable as well.

6.3 Comparison with Earlier Work

The secular stability of close binary systems has been discussed previously by Counselman (1973), Hut (1980) and others, in the limit where both stars can be represented by rigid spheres (i.e., neglecting spin-induced and tidal deformations). In this limit, the total angular momentum of a synchronized system is simply

$$J^{(S)}(r) = (\mu r^2 + I_o + I_o') \left(\frac{GM_t}{r^3}\right)^{1/2}, \tag{6.15}$$

where $M_t = M + M'$, $I_o = \frac{2}{5}\kappa_n M R_o^2$ and $I_o' = \frac{2}{5}\kappa_n' M' R_o'^2$. The corresponding total equilibrium energy is

$$E^{(S)}(r) = -\frac{GMM'}{2r} + \frac{1}{2}(I_o + I_o')\frac{GM_t}{r^3} + E_\infty, \tag{6.16}$$

where E_∞ is the energy at infinite separation. The secular stability limit r_m is the point at which $dE^{(S)}/dr = 0$, which gives

$$\mu r_m^2 = 3(I_o + I_o'). \tag{6.17}$$

The corresponding (minimum) value of J is

$$J_{min}^{(S)} = \frac{4}{3}\left[3\,G^2\mu^3 M_t^2(I_o + I_o')\right]^{1/4}. \tag{6.18}$$

Equations (6.15), (6.17), and (6.18) can be combined together with the requirement that $J > J_{min}$ (cf. §6.2.2) to show that synchronization is possible only when the orbital angular momentum exceeds the spin angular momentum by more than a factor of three (Counselman 1973; Hut 1980).

The above analysis applies only when tidal effects are small near r_m, which requires $r_m \gg R_o + R_o'$. Consider for simplicity the case where $I_o' \ll I_o$ (e.g., when M' is a point mass). Equation (6.17) implies that $r_m \sim R_o(1+M/M')^{1/2}$. So the inequality $r_m \gg R_o$ requires $M \gg M'$, i.e., the mass of the extended star must be much larger than that of its smaller-size companion (A typical example is provided by planet-satellite systems). When these inequalities are not satisfied, the simple analysis based on spheres is not valid, since tidal effects cannot be ignored.

Our general results agree with these early studies only in the limit where $p = M/M' \gg 1$. Values of r_m and J_{min} for different cases can be read off Table 2, and can be compared with equation (6.18). As expected, the differences are largest when p is close to unity. For example, for the case illustrated in Figure 9 (where $p = 0.85$), the two-sphere model (eqs. [6.17] and [6.18]) predicts $r_m/R_o \simeq 2.0$ and $\bar{J}_{min} \simeq 1.16$, whereas we find $r_m/R_o \simeq 3.0$ and $\bar{J}_{min} \simeq 1.28$. Even for large p, the rigid-sphere model can give incorrect results at small separation. Figure 12 shows a comparison between the two models for a system containing an incompressible star ($n = 0$) in orbit around a point mass, with $p = M/M' = 10$ (M' is the point mass). Constant$-J$ sequences with $J < J_{min}$, $J = J_{min}$ and $J > J_{min}$ are shown. Combining equations (6.15) and (6.16) and letting $I_o' = 0$, we find that the total energy along a constant$-J$ sequence is given by

$$E_J^{(S)}(r) = -\frac{GMM'}{2r} + \frac{1}{2I_o}\left[J - \mu r^2\left(\frac{GM_t}{r^3}\right)^{1/2}\right]^2 + E_\infty, \qquad (6.19)$$

in the rigid-sphere model. We see in Figure 12 that this result agrees with our calculations at large separation, but becomes invalid for small r. The expression correctly predicts the existence of a minimum and maximum residing on the synchronized curve given by equation (6.16). However, expression (6.19) does not exhibit the additional (third) energy extremum which corresponds to the onset of dynamical instability (cf. Fig. 11).

Acknowledgements

APPENDIX A: ASYMPTOTIC RESULTS FOR LARGE SEPARATION

As noted in §2.2, to quadrupole order, the only coupling between the equilibrium equations for two stars is through the orbital angular velocity Ω. For sufficiently large r, this coupling becomes very small (i.e., we can set $\delta \simeq 0$ and $\delta' \simeq 0$ in the equations). Thus to determine the structure of the star of mass M, we can treat M' as a point mass. The general Darwin-Riemann problem then reduces to the Roche-Riemann problem (LRS1, §8). Here we derive asymptotic results in the limit where $r \gg (1 + M'/M)^{1/3} R_o$ for various Roche-Riemann configurations. References to key equations in LRS1 are indicated with numbers preceded by an "I".

Index Symbols

We start by obtaining expressions for the index symbols A_i and related quantities for small deviations from a spherical shape. Let's rewrite the semi-major axes as

$$a_i \equiv R_o(1 + \alpha_i), \qquad \text{with } \alpha_i \ll 1. \tag{A1}$$

As we show below, the α_i are $\mathcal{O}(R_o^3/r^3)$ in general for large r. Expanding the integrand in the definition (2.8) we get

$$A_i = R_o^3(1 + \alpha_1 + \alpha_2 + \alpha_3) \int_0^\infty \left[1 - \frac{R_o^2}{R_o^2 + u}(\alpha_1 + \alpha_2 + \alpha_3 + 2\alpha_i) \right] \frac{du}{(R_o^2 + u)^{5/2}} + \mathcal{O}(\alpha_i{}^2) \tag{A2}$$

The integral is now elementary and we find

$$A_i = \frac{2}{3} + \frac{4}{15}(\alpha_1 + \alpha_2 + \alpha_3) - \frac{4}{5}\alpha_i + \mathcal{O}(\alpha_i{}^2) \tag{A3}$$

For spheroids with $a_1 = a_2 > a_3$ and $e^2 \equiv 1 - a_3^2/a_1^2 = 2(\alpha_1 - \alpha_3) + \mathcal{O}(\alpha_i{}^2)$ this becomes

$$\begin{aligned} A_1 = A_2 &= \frac{2}{3} - \frac{2}{15}e^2 + \mathcal{O}(e^4), \\ A_3 &= \frac{2}{3} + \frac{4}{15}e^2 + \mathcal{O}(e^4). \end{aligned} \tag{A4}$$

Related quantities of interest are (cf. eqs. [2.7] and [2.43])

$$f = \frac{1}{2} \frac{A_1 a_1^2 + A_2 a_2^2 + A_3 a_3^2}{(a_1 a_2 a_3)^{2/3}} = 1 + \mathcal{O}(\alpha_i{}^2), \tag{A5}$$

and

$$\begin{aligned} A_1 a_1^2 - A_3 a_3^2 &= (a_1^2 - a_3^2)B_{13} = \frac{8}{15}(\alpha_1 - \alpha_3)R_o^2, \\ A_2 a_2^2 - A_3 a_3^2 &= (a_2^2 - a_3^2)B_{23} = \frac{8}{15}(\alpha_2 - \alpha_3)R_o^2. \end{aligned} \tag{A6}$$

Maclaurin Spheroids

For future reference we first derive the α_i for a slowly rotating Maclaurin spheroid (LRS1, §3). We introduce the dimensionless angular velocity $\bar{\Omega}_s \equiv \Omega_s/(\pi G \bar{\rho}_o)^{1/2}$ as a small parameter in all expansions. As shown below we have $\alpha_i = \mathcal{O}(\bar{\Omega}_s^2) = \mathcal{O}(e^2)$.

We first expand expression (I.3.21) for the ratio $T/|W|$ and find

$$\frac{T}{|W|} = \frac{2}{15}e^2 + \mathcal{O}(e^4) = \frac{4}{15}(\alpha_1 - \alpha_3). \tag{A7}$$

Similarly, expression (I.3.8) gives $g = 1 + \mathcal{O}(e^4)$. Inserting these results into equation (I.3.25) gives the volume expansion factor to $\mathcal{O}(e^2)$,

$$\frac{a_1^2 a_3}{R_o^3} - 1 = 2\alpha_1 + \alpha_3 = \frac{8}{5}\left(\frac{n}{3-n}\right)(\alpha_1 - \alpha_3) = \frac{2}{15}\left(\frac{n}{3-n}\right)e^2. \tag{A8}$$

This is one equilibrium condition on α_1 and α_3. As a second equilibrium condition, we use the first of equations (I.3.27), together with expression (I.3.28) for $\hat{\Omega}$. Expanding these to $\mathcal{O}(e^2)$ we get

$$\hat{\Omega}^2 = \frac{8}{15}e^2 = \frac{16}{15}(\alpha_1 - \alpha_3) = q_n \bar{\Omega}_s^2. \tag{A9}$$

We can now solve equations (A8) and (A9) to obtain explicit $\mathcal{O}(\bar{\Omega}_s^2)$ relations for the volume expansion factor,

$$2\alpha_1 + \alpha_3 = \frac{3}{2}q_n\left(\frac{n}{3-n}\right)\bar{\Omega}_s^2, \tag{A10}$$

the eccentricity

$$e^2 = \frac{15}{8}q_n\bar{\Omega}_s^2, \tag{A11}$$

and the axes

$$\alpha_1 = \frac{3}{16}q_n\left(\frac{5+n}{3-n}\right)\bar{\Omega}_s^2,$$
$$\alpha_3 = -\frac{3}{8}q_n\left(\frac{5-3n}{3-n}\right)\bar{\Omega}_s^2. \tag{A12}$$

Roche Ellipsoids

Now turn to Roche ellipsoids (LRS1, §7). We first use equation (I.7.21) for the volume expansion factor, where the term containing $\delta = \mathcal{O}(R_o^5/r^5)$ can be neglected and we can set $f = 1$ (cf. eq. [A5]). Using

$$\frac{T_s}{|W|} = \frac{\frac{1}{2}I\Omega^2}{\dfrac{3}{5-n}\dfrac{GM^2}{R}} = \frac{1}{3}q_n\left(\frac{1+p}{p}\right)\frac{R_o^3}{r^3} + \mathcal{O}\left(\frac{R_o^6}{r^6}\right) \tag{A13}$$

we get

$$\frac{a_1 a_2 a_3}{R_o^3} - 1 = \alpha_1 + \alpha_2 + \alpha_3 = q_n\left(\frac{2n}{3-n}\right)\left(\frac{1+p}{p}\right)\frac{R_o^3}{r^3} + \mathcal{O}\left(\frac{R_o^6}{r^6}\right). \tag{A14}$$

We obtain two more equations for the α_i from the two equilibrium conditions (I.7.18) and (I.7.19). Since

$$\tilde{\mu} = \frac{GM'/r^3}{\pi GM/(\frac{4}{3}\pi R^3)} = \frac{4}{3}\frac{1}{p}\frac{R_o^3}{r^3} + \mathcal{O}\left(\frac{R_o^6}{r^6}\right), \tag{A15}$$

28

is already $\mathcal{O}(R_o^3/r^3)$, the terms inside the brackets need not be expanded. Using expressions (A6) we then find that the two equilibrium conditions can be written to this order as

$$
\begin{aligned}
\alpha_1 - \alpha_3 &= \frac{5}{4} q_n \left(\frac{4+p}{p} \right) \frac{R_o^3}{r^3}, \\
\alpha_2 - \alpha_3 &= \frac{5}{4} q_n \left(\frac{1+p}{p} \right) \frac{R_o^3}{r^3}.
\end{aligned}
\tag{A16}
$$

We now solve equations (A14) and (A16) for α_i, and find

$$
\begin{aligned}
\alpha_1 &= \frac{1}{3} q_n \left(\frac{1+p}{p} \right) \frac{R_o^3}{r^3} \left[\frac{5}{4} \left(\frac{7+p}{1+p} \right) + \left(\frac{2n}{3-n} \right) \right] \\
\alpha_2 &= -\frac{1}{3} q_n \left(\frac{1+p}{p} \right) \frac{R_o^3}{r^3} \left[\frac{5}{4} \left(\frac{2-p}{1+p} \right) - \left(\frac{2n}{3-n} \right) \right] \\
\alpha_3 &= -\frac{1}{3} q_n \left(\frac{1+p}{p} \right) \frac{R_o^3}{r^3} \left[\frac{5}{4} \left(\frac{5+2p}{1+p} \right) - \left(\frac{2n}{3-n} \right) \right]
\end{aligned}
\tag{A17}
$$

It is also useful to obtain lowest-order changes in the total equilibrium energy and angular momentum of the binary system. These are defined with respect to a ficticious (nonequilibrium) system containing two spherical (nonspinning) polytropes in a point-like Keplerian orbit,

$$
\begin{aligned}
\Delta E_{eq} &\equiv E_{eq} - \left[\frac{1}{2} \mu r^2 \Omega_K^2 - \frac{GMM'}{r} + \left(\frac{3-n}{3} \right) W_o \right], \\
\Delta J_{eq} &\equiv J_{eq} - \mu r^2 \Omega_K,
\end{aligned}
\tag{A18}
$$

where $W_o \equiv -[3/(5-n)]GM^2/R_o$ is the self-gravitational energy of the spherical polytrope and $\Omega_K^2 = G(M+M')/r^3$. Using equation (I.7.11) for E_{eq} we get

$$
\begin{aligned}
\Delta E_{eq} &= \frac{1}{2} \mu r^2 \Omega_K^2 \delta - \frac{GMM'}{r} \left(\frac{2n+3}{9} \right) \delta + \left(\frac{3-n}{3} \right) W_o \left(\frac{R_o}{r} - 1 \right) + \left(\frac{3-2n}{3} \right) T_s \\
&= \left[\left(\frac{3-n}{3} \right) W_o \left(\frac{R_o}{r} - 1 \right) + \left(\frac{3-2n}{3} \right) T_s \right] \left[1 + \mathcal{O} \left(\frac{R_o^3}{r^3} \right) \right].
\end{aligned}
\tag{A19}
$$

We now substitute $T_s = \frac{1}{2} I_o \Omega_K^2$, with $I_o = \frac{2}{5} \kappa_n M R_o^2$, (to lowest order) and expression (A14) for $R = (a_1 a_2 a_3)^{1/3}$ to find

$$
\begin{aligned}
\Delta E_{eq} &= \left[\frac{2n}{15} \kappa_n R_o^2 M \frac{G(M+M')}{r^3} + \frac{1}{5} \left(1 - \frac{2n}{3} \right) \kappa_n R_o^2 M \frac{G(M+M')}{r^3} \right] \left[1 + \mathcal{O} \left(\frac{R_o^3}{r^3} \right) \right] \\
&= \frac{1}{2} I_o \Omega_K^2 \left[1 + \mathcal{O} \left(\frac{R_o^3}{r^3} \right) \right].
\end{aligned}
\tag{A20}
$$

To lowest order, this is just the naive result that one would have written down immediately while ignoring the virial theorem. For the angular momentum equations (I.7.12) and (A18) give immediately

$$
\Delta J_{eq} = I_o \Omega_K \left[1 + \mathcal{O} \left(\frac{R_o^3}{r^3} \right) \right].
\tag{A21}
$$

29

It is useful to note that (1) ΔJ_{eq} is considerably easier to calculate than ΔE_{eq}, and (2) once an expression has been derived for ΔJ_{eq}, ΔE_{eq} can be obtained very simply by integrating the relation $dE_{eq} = \Omega\, dJ_{eq}$ (cf. LRS1, Appendix D). Indeed, using expression (A21) we find, to lowest order,

$$\Delta E_{eq} = \int \Omega_K \frac{d\Delta J_{eq}}{dr}\, dr = -\frac{3}{2} I_o G(M + M') \int \frac{dr}{r^4} = \frac{1}{2} I_o \Omega_K^2 \qquad (A22),$$

in agreement with expression (A20). For the more general configurations considered below, the calculation of ΔE_{eq} by direct expansion of E_{eq} would be extremely tedious, and we will instead use this shortcut.

Our results (A17), (A20), and (A21) are in agreement with those quoted by Kochanek (1992, cf. his eqs. [2.5] and [2.6]), with his quantity $\hat{\Omega}_o^2$ equal to $q_n[(1+p)/p](R_o^3/r_3)$ in our notations (and his $I_* = I_o/2$).

Irrotational Roche-Riemann Ellipsoids

From equation (I.8.2) with $\Lambda = 2a_1 a_2 \Omega/(a_1^2 + a_2^2)$ for irrotational configurations we see immediately that $T_s = T_+ + T_- \propto (a_1 - a_2)^2 \propto R_o^2(\alpha_1 - \alpha_2)^2$ and therefore that $T_s/|W| = \mathcal{O}(R_o^6/r^6)$. Thus from equation (I.7.21) we see that there is no change of volume to lowest order,

$$\alpha_1 + \alpha_2 + \alpha_3 = 0. \qquad (A23)$$

With $Q_1 = -Q_2 = \Omega_K[1 + \mathcal{O}(R^6/r^6)]$ and $\Omega_K^2 = \mu_R(1 + p)$, the two equilibrium conditions (I.8.5) and (I.8.6) give to this order

$$\alpha_1 - \alpha_3 = \frac{15}{4} q_n \frac{1}{p} \frac{R_o^3}{r^3},$$

$$\alpha_2 - \alpha_3 = 0. \qquad (A24)$$

Combining equations (A23) and (A24) we find

$$\alpha_1 = \frac{5}{2} q_n \frac{1}{p} \frac{R_o^3}{r^3},$$

$$\alpha_2 = \alpha_3 = -\frac{5}{4} q_n \frac{1}{p} \frac{R_o^3}{r^3}, \qquad (A25)$$

in agreement with the results quoted by Kochanek (1992;cf. his eq. [2.7]).

Using equation (I.8.3) with $f_R = -2$ and the definition (A18) we get for the change in angular momentum,

$$\Delta J_{eq} = \frac{1}{2}\mu r^2 \Omega_K \delta + \left(I - 4\frac{I_{11}I_{22}}{I}\right)\Omega_K. \qquad (A26)$$

Since $I_{ii} = I_o(1 + 2\alpha_i)/2$ and $I = I_{11} + I_{22} = I_o(1 + \alpha_1 + \alpha_2)$, we see that the second term in expression (A26) is of higher order. Using the results (A25) and the definition (I.7.7) we get

$$\delta = \frac{3}{5}\kappa_n \frac{R_o^2}{r^2}(2\alpha_1 - \alpha_2 - \alpha_3) = \frac{9}{2}\frac{\kappa_n q_n}{p}\frac{R_o^5}{r^5}, \qquad (A27)$$

and equation (A26) gives

$$\Delta J_{eq} = \frac{45}{8}\frac{q_n}{p(1+p)}R_o^3\, r^3 I_o \Omega_K$$

$$= \frac{9}{4}\kappa_n q_n M'^2 \left(\frac{G}{M + M'}\right)^{1/2}\frac{R_o^5}{r^{9/2}} \qquad (A28)$$

30

We now evaluate the change in total energy using the trick described above. Writing $\Omega = \Omega_K + \Delta\Omega$, with $\Delta\Omega = \Omega_K\delta/2$, and expanding the relation $dE_{eq} = \Omega dJ_{eq}$ to lowest order we get

$$\Delta E_{eq} = \int \left(\Omega_K \frac{d\Delta J_{eq}}{dr} + \Delta\Omega \frac{dJ_o}{dr} \right) dr, \tag{A29}$$

where $J_o = \mu r^2 \Omega_K$. Combining equations (A27)–(A29) we find

$$\begin{aligned}
\Delta E_{eq} &= \frac{15}{4} \frac{q_n}{p(1+p)} \frac{R_o^3}{r^3} I_o \Omega_K^2, \\
&= \frac{3}{2} \kappa_n q_n GM'^2 \frac{R_o^5}{r^6}.
\end{aligned} \tag{A30}$$

This does not agree with the result quoted by Kochanek (1992; see his eq. [2.8], which appears to differ in both the magnitude and sign of the numerical coefficient).

General Roche-Riemann Ellipsoids

In the limit of small tidal perturbation and slow spin, the deviation of a general Roche-Riemann ellipsoid from a sphere can be written as a linear superposition of a pure tidal distortion and a distortion purely due to the spin. Thus the lowest-order expressions for the principal axes are obtained simply by adding expressions (A12) and (A25). The value of $\bar{\Omega}_s$ is determined by the condition that the circulation $\mathcal{C} = -I_o\Omega_s$ at large r (cf. eqs. [2.54]).

The lowest-order changes in energy and angular momentum due to spin are simply $\Delta E_{eq}^{(S)} = \frac{1}{2}I_o\Omega_s^2$ and $\Delta J_{eq}^{(S)} = I_o\Omega_s$, which are both independent of r. For the calculation of gravitational radiation phase shifts (cf. §4.3 and LRS3), it is necessary to obtain the next higher-order, r-dependent term in the expansion of E_{eq}. This is done most easily using the same method as above, first calculating ΔJ_{eq} and then integrating $dE_{eq} = \Omega \, dJ_{eq}$. By direct expansion of expression (I.8.3) we find

$$\Delta J_{eq}^{(S)} = I_o\Omega_s \left[1 + \frac{3}{8}q_n \left(\frac{5+n}{3-n} \right) \bar{\Omega}_s^2 \right] + I_o\Omega_K \left(\frac{45}{64} \frac{q_n}{1+p} \bar{\Omega}_s^2 \right). \tag{A31}$$

Using equation (A29) we then get, after some algebra,

$$\Delta E_{eq}^{(S)} = \frac{3}{32} \kappa_n q_n GMM' \bar{\Omega}_s^2 \frac{R_o^3}{r^3} + \text{ const.} \tag{A32}$$

The total ΔE_{eq} is obtained by adding expressions (A30) and (A32).

APPENDIX B: SECOND DERIVATIVES OF THE ENERGY FUNCTION

Dynamical Stability Limit

To obtain the dynamical stability limit using equation (3.1), we need to evaluate the second derivatives of the energy function with respect to $\{\alpha_i\} = \{r, \rho_c, \lambda_1, \lambda_2, \rho_c', \lambda_1{}', \lambda_2{}'\}$ while holding J, $\mathcal{C}$ and $\mathcal{C}'$ fixed. We adopt the notation of Appendix A of LRS1, where many of the useful algebraic expressions are given. Using the energy function (2.29) we obtain the first derivatives of the energy function as

$$
\begin{aligned}
\frac{\partial E}{\partial r} &= -\mu r \Omega^2 + \frac{GMM'}{r^2} + \frac{3GM'\delta I}{2r^4} + \frac{3GM\delta I'}{2r^4}, \\
\frac{\partial E}{\partial \rho_c} &= \frac{1}{n\rho_c}U + \frac{1}{3\rho_c}W + \frac{2}{3\rho_c}T_s + \frac{1}{3\rho_c}\frac{GM'\delta I}{r^3}, \\
\frac{\partial E}{\partial \lambda_1} &= \frac{h_{+(1)}}{\lambda_1}T_+ + \frac{h_{-(1)}}{\lambda_1}T_- + \frac{\mathcal{I}_{(1)}}{\lambda_1}W + \frac{GM'}{2r^3\lambda_1}(4I_{11} + I_{22} + I_{33}), \\
\frac{\partial E}{\partial \lambda_2} &= \frac{h_{+(2)}}{\lambda_2}T_+ + \frac{h_{-(2)}}{\lambda_2}T_- + \frac{\mathcal{I}_{(2)}}{\lambda_2}W - \frac{GM'}{2r^3\lambda_2}(2I_{11} + 2I_{22} - I_{33}),
\end{aligned}
\tag{B1}
$$

where we have defined $\delta I \equiv 2I_{11} - I_{22} - I_{33}$ and similarly for $\delta I'$. The other first derivatives $\partial E/\partial \rho_c'$, $\partial E/\partial \lambda_1'$, and $\partial E/\partial \lambda_2{}'$ can be obtained from $\partial E/\partial \rho_c$, $\partial E/\partial \lambda_1$, and $\partial E/\partial \lambda_2$, respectively, by interchanging the unprimed quantities and the primed quantities. In equations (B1), we write $T_\pm$ and $T_\pm'$ as (cf. eq. [2.32])

$$
\begin{aligned}
T_\pm &= h_\pm \frac{(J_s \pm \mathcal{C})^2}{4I_s}, \\
T_\pm' &= h_\pm' \frac{(J - \mu r^2 \Omega - J_s \pm \mathcal{C}')^2}{4I_s'}.
\end{aligned}
\tag{B2}
$$

Note that both Ω and J_s are functions of the adopted variables $\{\alpha_i\}$ and the conserved quantities J, $\mathcal{C}$, $\mathcal{C}'$. The expression for $\Omega(\alpha_i; J, \mathcal{C}, \mathcal{C}')$ is given by equation (2.30); the expression for J_s can be obtained from equation (2.21) as

$$
J_s(\alpha_i; J, \mathcal{C}, \mathcal{C}') = \frac{2}{h_+ + h_-}I_s\Omega(\alpha_i; J, \mathcal{C}, \mathcal{C}') - \frac{h_+ - h_-}{h_+ + h_-}\mathcal{C}.
\tag{B3}
$$

To calculate the second derivatives of the energy function, we first calculate $(\partial\Omega/\partial\alpha_i)$ and $(\partial J_s/\partial\alpha_i)$, then we use

$$
\left(\frac{\partial^2 E}{\partial\alpha_i\partial\alpha_j}\right)_{J,\mathcal{C},\mathcal{C}'} = \left[\frac{\partial}{\partial\alpha_i}\left(\frac{\partial E}{\partial\alpha_j}\right)\right]_{\Omega,J_s} + \left[\frac{\partial}{\partial\Omega}\left(\frac{\partial E}{\partial\alpha_j}\right)\right]\left(\frac{\partial\Omega}{\partial\alpha_i}\right) + \left[\frac{\partial}{\partial J_s}\left(\frac{\partial E}{\partial\alpha_j}\right)\right]\left(\frac{\partial J_s}{\partial\alpha_i}\right).
\tag{B4}
$$

For convenience, we define

$$
\begin{aligned}
I_h &\equiv I_s/(h_+ + h_-), \\
I_e &\equiv \mu r^2 + 2(I_h + I_h'), \\
F_d &\equiv -1 + 2I_h/I_e, \\
I_c &\equiv I_h I_h'/I_e, \\
\Sigma_i &\equiv h_{+(i)}(\Omega + \Lambda) + h_{-(i)}(\Omega - \Lambda), \quad i = 1, 2,
\end{aligned}
\tag{B5}
$$

and similarly for I'_h, F'_d and Σ'_i. We obtain the following expressions:

$$r^2\left(\frac{\partial^2 E}{\partial r^2}\right) = -\mu r^2\Omega^2 - \frac{2GMM'}{r} - \frac{6GM'\delta I}{r^3} - \frac{6GM\delta I'}{r^3} - (2\mu r^2\Omega)\left(-\frac{2\mu r^2}{I_e}\Omega\right),$$

$$r\rho_c\left(\frac{\partial^2 E}{\partial r\partial\rho_c}\right) = -\frac{GM'\delta I}{r^3} - (2\mu r^2\Omega)\frac{4I_h}{3I_e}\Omega,$$

$$r\lambda_1\left(\frac{\partial^2 E}{\partial r\partial\lambda_1}\right) = -\frac{3GM'}{2r^3}(4I_{11}+I_{22}+I_{33}) - (2\mu r^2\Omega)\frac{I_h}{I_e}\Sigma_1,$$

$$r\lambda_2\left(\frac{\partial^2 E}{\partial r\partial\lambda_2}\right) = \frac{3GM'}{2r^3}(2I_{11}+2I_{22}-I_{33}) - (2\mu r^2\Omega)\frac{I_h}{I_e}\Sigma_2,$$

$$\rho_c^2\left(\frac{\partial^2 E}{\partial\rho_c^2}\right) = \frac{1}{3}\left[\left(\frac{1}{3}-\frac{1}{n}\right)W + 2\left(\frac{2}{3}-\frac{1}{n}\right)T_s - \left(\frac{2}{3}+\frac{1}{n}\right)\frac{GM'\delta I}{r^3}\right] + \frac{2\Omega}{3}\frac{4I_h\Omega}{3}F_d,$$

$$\rho_c\lambda_1\left(\frac{\partial^2 E}{\partial\rho_c\partial\lambda_1}\right) = \frac{2}{3}(h_{+(1)}T_+ + h_{-(1)}T_-) + \frac{\mathcal{I}_{(1)}}{3}W - \frac{GM'}{3r^3}(4I_{11}+I_{22}+I_{33}) + \frac{2\Omega}{3}I_h\Sigma_1 F_d,$$

$$\rho_c\lambda_2\left(\frac{\partial^2 E}{\partial\rho_c\partial\lambda_2}\right) = \frac{2}{3}(h_{+(2)}T_+ + h_{-(2)}T_-) + \frac{\mathcal{I}_{(2)}}{3}W + \frac{GM'}{3r^3}(2I_{11}+2I_{22}-I_{33}) + \frac{2\Omega}{3}I_h\Sigma_2 F_d,$$

$$\rho_c\rho'_c\left(\frac{\partial^2 E}{\partial\rho_c\rho'_c}\right) = \frac{2\Omega}{3}\left(\frac{8I_c\Omega}{3}\right),$$

$$\rho_c\lambda_1'\left(\frac{\partial^2 E}{\partial\rho_c\lambda_1'}\right) = \frac{2\Omega}{3}(2I_c\Sigma_1'),$$

$$\rho_c\lambda_2'\left(\frac{\partial^2 E}{\partial\rho_c\lambda_2'}\right) = \frac{2\Omega}{3}(2I_c\Sigma_2'),$$

$$\lambda_1^2\left(\frac{\partial^2 E}{\partial\lambda_1^2}\right) = h_{+(11)}T_+ + h_{-(11)}T_- + \mathcal{I}_{(11)}W - \frac{6GM'I_{11}}{r^3} + \frac{\Sigma_1}{2}I_h\Sigma_1 F_d,$$

$$\lambda_1\lambda_2\left(\frac{\partial^2 E}{\partial\lambda_1\lambda_2}\right) = h_{+(12)}T_+ + h_{-(12)}T_- + \mathcal{I}_{(12)}W + \frac{GM'}{2r^3}(4I_{11}-2I_{22}+I_{33}) + \frac{\Sigma_1}{2}I_h\Sigma_2 F_d,$$

$$\lambda_1\lambda_1'\left(\frac{\partial^2 E}{\partial\lambda_1\lambda_1'}\right) = \frac{\Sigma_1}{2}(2I_c\Sigma_1'),$$

$$\lambda_1\lambda_2'\left(\frac{\partial^2 E}{\partial\lambda_1\lambda_2'}\right) = \frac{\Sigma_1}{2}(2I_c\Sigma_2'),$$

$$\lambda_2^2\left(\frac{\partial^2 E}{\partial\lambda_2^2}\right) = h_{+(22)}T_+ + h_{-(22)}T_- + \mathcal{I}_{(22)}W + \frac{3GM'I_{22}}{r^3} + \frac{\Sigma_2}{2}I_h\Sigma_2 F_d,$$

$$\lambda_2\lambda_2'\left(\frac{\partial^2 E}{\partial\lambda_2\partial\lambda_2'}\right) = \frac{\Sigma_2}{2}(2I_c\Sigma_2').$$

$$(B6)$$

The other independent matrix elements can be obtained by interchanging primed quantities and unprimed quantities in the appropriate expression given above. For example, $r\rho'_c(\partial^2 E/\partial r\partial\rho'_c)$ can be directly obtained from the expression for $r\rho_c(\partial^2 E/\partial r\partial\rho_c)$ given above, giving

$$r\rho'_c\left(\frac{\partial^2 E}{\partial r\partial\rho'_c}\right) = -\frac{GM\delta I'}{r^3} - (2\mu r^2\Omega)\frac{4I'_h}{3I_e}\Omega. \qquad (B7)$$

The expressions for $h_{\pm(i)}$, $\mathcal{I}_{(i)}$, $h_{\pm(ij)}$ and $\mathcal{I}_{(ij)}$ are given in Appendix A of LRS1.

Secular Stability Limit

To obtain the secular stability limit along a synchronized sequence using equation (3.1), we need to evaluate the second derivative of the energy function with respect to $\{\alpha_i\}$ with J fixed and holding $f_R = f'_R = 0$. In this case, equation (2.53) should be used for the kinetic energy term.

We define

$$
\begin{aligned}
I_t &\equiv \mu r^2 + I + I', \\
F_s &\equiv -1 + I/I_t,
\end{aligned}
\tag{B8}
$$

and similarly for F'_s. The second derivatives of the energy function are then given by:

$$
\begin{aligned}
r^2 \left(\frac{\partial^2 E}{\partial r^2} \right) &= -\mu r^2 \Omega^2 - \frac{2GMM'}{r} - \frac{6GM'\delta I}{r^3} - \frac{6GM\delta I'}{r^3} - (2\mu r^2 \Omega) \left(-\frac{2\mu r^2}{I_t} \Omega \right), \\
r\rho_c \left(\frac{\partial^2 E}{\partial r \partial \rho_c} \right) &= -\frac{GM'\delta I}{r^3} - (2\mu r^2 \Omega) \frac{2I}{3I_t} \Omega, \\
r\lambda_1 \left(\frac{\partial^2 E}{\partial r \partial \lambda_1} \right) &= -\frac{3GM'}{2r^3}(4I_{11} + I_{22} + I_{33}) - (2\mu r^2 \Omega) \frac{I}{I_t} h_{(1)} \Omega, \\
r\lambda_2 \left(\frac{\partial^2 E}{\partial r \partial \lambda_2} \right) &= \frac{3GM'}{2r^3}(2I_{11} + 2I_{22} - I_{33}) - (2\mu r^2 \Omega) \frac{I}{I_t} h_{(2)} \Omega, \\
\rho_c^2 \left(\frac{\partial^2 E}{\partial \rho_c^2} \right) &= \frac{1}{3} \left[\left(\frac{1}{3} - \frac{1}{n} \right) W + 2 \left(\frac{2}{3} - \frac{1}{n} \right) T_s - \left(\frac{2}{3} + \frac{1}{n} \right) \frac{GM'\delta I}{r^3} \right] + \frac{2\Omega}{3} \frac{2I\Omega}{3} F_s, \\
\rho_c \lambda_1 \left(\frac{\partial^2 E}{\partial \rho_c \partial \lambda_1} \right) &= \frac{2}{3} h_{(1)} T_s + \frac{\mathcal{I}_{(1)}}{3} W - \frac{GM'}{3r^3}(4I_{11} + I_{22} + I_{33}) + \frac{2\Omega}{3} h_{(1)} I\Omega F_s, \\
\rho_c \lambda_2 \left(\frac{\partial^2 E}{\partial \rho_c \partial \lambda_2} \right) &= \frac{2}{3} h_{(2)} T_s + \frac{\mathcal{I}_{(2)}}{3} W + \frac{GM'}{3r^3}(2I_{11} + 2I_{22} - I_{33}) + \frac{2\Omega}{3} h_{(2)} I\Omega F_s, \\
\rho_c \rho'_c \left(\frac{\partial^2 E}{\partial \rho_c \rho'_c} \right) &= \frac{2\Omega}{3} \frac{2II'\Omega}{3I_t}, \\
\rho_c \lambda_1' \left(\frac{\partial^2 E}{\partial \rho_c \lambda_1'} \right) &= \frac{2\Omega}{3} h'_{(1)} \frac{II'\Omega}{I_t}, \\
\rho_c \lambda_2' \left(\frac{\partial^2 E}{\partial \rho_c \lambda_2'} \right) &= \frac{2\Omega}{3} h'_{(2)} \frac{II'\Omega}{I_t}, \\
\lambda_1^2 \left(\frac{\partial^2 E}{\partial \lambda_1^2} \right) &= h_{(11)} T_s + \mathcal{I}_{(11)} W - \frac{6GM'I_{11}}{r^3} + (h_{(1)}\Omega) h_{(1)} I\Omega F_s, \\
\lambda_1 \lambda_2 \left(\frac{\partial^2 E}{\partial \lambda_1 \lambda_2} \right) &= h_{(12)} T_s + \mathcal{I}_{(12)} W + \frac{GM'}{2r^3}(4I_{11} - 2I_{22} + I_{33}) + (h_{(1)}\Omega) h_{(2)} I\Omega F_s, \\
\lambda_1 \lambda_1' \left(\frac{\partial^2 E}{\partial \lambda_1 \lambda_1'} \right) &= (h_{(1)}\Omega) h'_{(1)} \frac{II'\Omega}{I_t}, \\
\lambda_1 \lambda_2' \left(\frac{\partial^2 E}{\partial \lambda_1 \lambda_2'} \right) &= (h_{(1)}\Omega) h'_{(2)} \frac{II'\Omega}{I_t}, \\
\lambda_2^2 \left(\frac{\partial^2 E}{\partial \lambda_2^2} \right) &= h_{(22)} T_s + \mathcal{I}_{(22)} W + \frac{3GM'I_{22}}{r^3} + (h_{(2)}\Omega) h_{(2)} I\Omega F_s, \\
\lambda_2 \lambda_2' \left(\frac{\partial^2 E}{\partial \lambda_2 \partial \lambda_2'} \right) &= (h_{(2)}\Omega) h'_{(2)} \frac{II'\Omega}{I_t}.
\end{aligned}
\tag{B9}
$$

Again, the other independent matrix elements can be obtained by interchanging primed quantities

34

and unprimed quantities in the appropriate expression given above. The expressions for $h_{(i)}$ and $h_{(ij)}$ are given in Appendix A of LRS1.

REFERENCES

Abramovici, A. et al. 1992, Science, 256, 325

Aizenman, M. L. 1968, ApJ, 153, 511

Alexander, M. E. 1973, Astron. Space Sci., 23, 459

Bailyn, C.D. 1993, in Dynamics of Globular Clusters: a Workshop in Honor of I.R. King, eds. S. Djorgovski & G. Meylan, ASP Conf. Series, in press

Bildsten, L., & Cutler, C. 1992, ApJ, 400, 175

Burrows, A., & Liebert, J. 1993, Rev. Mod. Phys., 65, 301

Chandrasekhar, S. 1939, An Introduction to the Study of Stellar Structure, (Chicago: The University of Chicago Press).

Chandrasekhar, S. 1969, Ellipsoidal Figures of Equilibrium (New Haven: Yale University Press) (Ch69)

Chen, K, & Leonard, P. J. T. 1993, ApJL, 411, L75

Clark, J. P. A., & Eardley, D. M. 1977, ApJ, 251, 311

Counselman, C. C. 1973, ApJ, 180, 307

D'Antona, F. 1987, ApJ, 320, 653

Evans, C. R., Iben, I., & Smarr, L. 1987, ApJ, 323, 129

Hachisu, I. 1986, ApJS, 62, 461

Hachisu, I., & Eriguchi, Y. 1984a, Pub. Astron. Soc. Japan, 36, 239

Hachisu, I., & Eriguchi, Y. 1984b, Pub. Astron. Soc. Japan, 36, 259

Hut, P. 1980, A&A, 92, 167

Iben, I., & Tutukov, A. V. 1984, ApJS, 54, 335

Jaranowski, P., & Krolak, A. 1992, ApJ, 394, 586

Kochanek, C. S. 1992, ApJ, 398, 234

Kopal, Z. 1959, Close Binary Systems (London: Chapman & Hall)

Lai, D., Abrahams, A. M., & Shapiro, S. L. 1991, ApJ, 377, 612

Lai, D., Rasio, F. A., & Shapiro, S. L. 1993a, ApJS, in press (LRS1)

Lai, D., Rasio, F. A., & Shapiro, S. L. 1993b, ApJL, 406, L63 (LRS2)

Lai, D., Rasio, F. A., & Shapiro, S. L. 1993c, ApJ, in press (LRS3)

Landau, L. D., & Lifshitz, E. M. 1987, Fluid Mechanics, 2nd Ed. (Oxford: Pergamon Press)

Levine, A., Rappaport, S., Putney, A., Corbet, R., & Nagase, F. 1991, ApJ, 381, 101

Levine, A., Rappaport, S., Deeter, J. E., Boynton, P. E., & Nagase, F. 1993, ApJ, in press

Mateo, M., Harris, H. C., Nemec, J., & Olszewski, E. W. 1990, AJ, 100, 469

Miller, B. D. 1974, ApJ, 187, 609

Narayan, R., Paczyński, B., & Piran, T. 1992, ApJL, 395, L83

Ostriker, J. P. & Gunn, J. E. 1969, ApJ, 157, 1395

Press, W. H., Flannery, B. P., Teukolsky, S. A., & Vetterling, W. T. 1987 Numerical Recipes: The Art of Scientific Computing (Cambridge: Cambridge Univ. Press)

Rasio, F. A. 1993, in Proceedings of International Workshop on Evolutionary Links in the Zoo of Interacting Binaries, ed. F. D'Antona, Mem. Soc. Astron. Ital., in press

Rasio, F. A., & Shapiro, S. L. 1992, ApJ, 401, 226

Rasio, F. A., & Shapiro, S. L. 1993, in preparation

Shapiro, S. L., & Teukolsky, S. A. 1983, Black Holes, White Dwarfs, and Neutron Stars (New York: Wiley)

Tassoul, J.-L. 1978, Theory of Rotating Stars (Princeton: Princeton University Press)

Usov, V. V. 1992, Nature, 357, 472

Wiringa, R. B., Fiks, V., & Fabrocini, A. 1988, Phys. Rev., C38, 1010

Zahn, J.-P. 1977, A&A, 57, 383

Zapolsky, H. S., and Salpeter, E. E. 1969, ApJ, 158, 809

FIGURE CAPTIONS

FIG. 1.— Equilibrium curves of total energy E, angular momentum J, and orbital angular velocity Ω as a function of r along selected Darwin-Riemann sequences. All sequences have $K = K'$, $n = n' = 1.5$, and $f_R = f_R' = 0$ (synchronized spins). Curves corresponding to different values of the mass ratio $p = M/M'$ are shown: $p = 1$ (solid lines), $p = 0.8$ (dotted lines), $p = 0.6$ (short-dashed lines) and $p = 0.5$ (long-dashed lines). To obtain convergence of all the curves at large r, the units of energy and angular momentum are chosen to be $E_c \equiv GMM'/(R_o + R_o')$ and $J_c \equiv [GM^2M'^2(R_o + R_o')/(M + M')]^{1/2}$. The quantities $E_\infty = -[(3 - n)/(5 - n)]GM^2/R_o - [(3 - n')/(5 - n')]GM'^2/R_o'$ and $\Omega_K^2 = G(M + M')/r^3$ have been subtracted for convenience.

FIG. 2.— Equilibrium curves of total energy as a function of binary separation along selected Darwin-Riemann sequences containing two identical components with $n = 0$. The solid line is for the synchronized sequence, the dotted lines are for constant-circulation sequences with, from top to bottom, $2\mathcal{C}/(GM^3R_o)^{1/2} = -0.32, -0.2832, -0.16$, and 0, corresponding to $\Omega_s/(GM/R_o^3)^{1/2} = 0.4, 0.354, 0.2$, and 0. The sequence having $2\mathcal{C}/(GM^3R_o)^{1/2} = -0.2832$ (slightly thicker dotted line) has an energy minimum located precisely on the synchronized sequence. This point (solid round dot) marks the onset of dynamical instability along the synchronized sequence. The energy minima mark the onset of secular instability along the synchronized sequence and dynamical instability along the constant$-\mathcal{C}$ sequences. The thick dashed line connects the dynamical stability limits of all constant$_\mathcal{C}$ sequences. It represents the boundary of the region containing dynamically stable equilibrium configurations in the (E, r) plane.

FIG. 3.— General classification of equilibrium sequences according to terminal configurations and stability limits. The existence and ordering of the secular stability limits (round dots), dynamical stability limits (square dots), and Roche limits (triangles) is shown schematically along equilibrium energy curves. The curves terminate at the contact solution.

FIG. 4.— Diagrams distinguishing the different regimes illustrated in Fig. 3 for synchronized models with (i) $K = K'$ (low-mass white dwarfs and planets), (ii) $R_o/R_o' = M/M'$ (low-mass

main-sequence stars), and (iii) $R_o = R'_o$ (neutron stars and brown dwarfs). All models have $n = n'$.

FIG. 5.— Same as Fig. 4, but here for irrotational configurations ($f_R = f'_R = -2$) with (i) $K = K'$ and (ii) $R_o = R'_o$, all with $n = n'$.

FIG. 6.— Same as Fig. 4, but here for synchronized Roche-Riemann configurations with $p = M/M' < 1$ (i.e., the point mass is more massive than its finite-size companion). In many cases, Darwin-Riemann configurations approach Roche-Riemann configurations as $p \to 0$ (see text).

FIG. 7.— Comparison between our results for incompressible Darwin models and those of Hachisu & Eriguchi (1984b). Mass ratios $p = M/M' = 1.5$, 5, and 10 have been considered. The square of the orbital frequency Ω^2 is plotted as a function of the total angular momentum J in the system. The units are defined in eqs. (4.1). The solid lines show our results, the dots are from Table 1 of HE.

FIG. 8.— Comparison between our results for models of main-sequence star binaries and those of recent SPH calculations. All models have $n = n' = 1.5$ and polytropic constants such that $R_o/M = R'_o/M'$. Mass ratios $p = 1.0$, 0.75, 0.5, and 0.25 are considered. The dashed lines show our quasi-analytic results, the solid lines were determined using SPH. The onset of Roche lobe overflow as determined by SPH is indicated by the thick vertical line segments marked RL. The point of first contact along the SPH sequence with $p = 1.0$ is indicated by the thin vertical segment marked C.

FIG. 9.— Comparison between our results and those of recent SPH calculations for models with $n = n' = 0.5$, $K = K'$, and $p = M/M' = 0.85$. Conventions are as in Fig. 8. The dynamical stability limit determined by SPH is indicated by the short vertical dashed line. The thin dashed line to the right shows the corresponding result for a binary model containing two rigid spheres (cf. §6.3).

FIG. 10.— Equilibrium curves of total angular momentum and energy for constant$-J$ sequences of Darwin-Riemann configurations with $n = n' = 1.5$ and $M = M'$ In (a), the short-dashed lines are for $J/(GM^3R_o)^{1/2} = 1.34$, the dotted lines for $J/(GM^3R_o)^{1/2} = 1.3202$, and the long-dashed lines for $J/(GM^3R_o)^{1/2} = 1.30$. The solid lines show the synchronized sequence for comparison. The regions around points B and C are magnified in the inserts. In (b), the dashed lines correspond to $J/(GM^3R_o)^{1/2} = 1.323$.

FIG. 11.— Same as Fig. 10, but for binaries with $n = n' = 0$ and $M = M'$. The short-dashed lines are for $J/(GM^3R_o)^{1/2} = 1.6$, the dotted lines for $J/(GM^3R_o)^{1/2} = 1.523$, and the long-dashed lines for $J/(GM^3R_o)^{1/2} = 1.45$. The solid lines show the synchronized sequence. The thick dashed lines indicate the dynamical stability limit.

FIG. 12.— Equilibrium curves of total angular momentum and energy for constant$-J$ sequences of Roche-Riemann configurations with $n = 0$ and $p = M/M' = 10$. The short-dashed lines are for $J/(GM^3R_o)^{1/2} = 0.25$, the dotted lines for $J/(GM^3R_o)^{1/2} = 0.2438$, and the long-dashed lines for $J/(GM^3R_o)^{1/2} = 0.25$. The solid lines correspond to the synchronized sequence. The thicker lines show our ellipsoidal results, while the lighter lines show the results obtained when the star is modeled as a rigid sphere (see text).

(i) $K = K'$

(ii) $R_o/R'_o = M/M'$

(iii) $R_o = R'_o$

$p = M/M'$

n

(i) $K = K'$

(ii) $R_o = R_o'$

$p = M/M'$

n

(a)
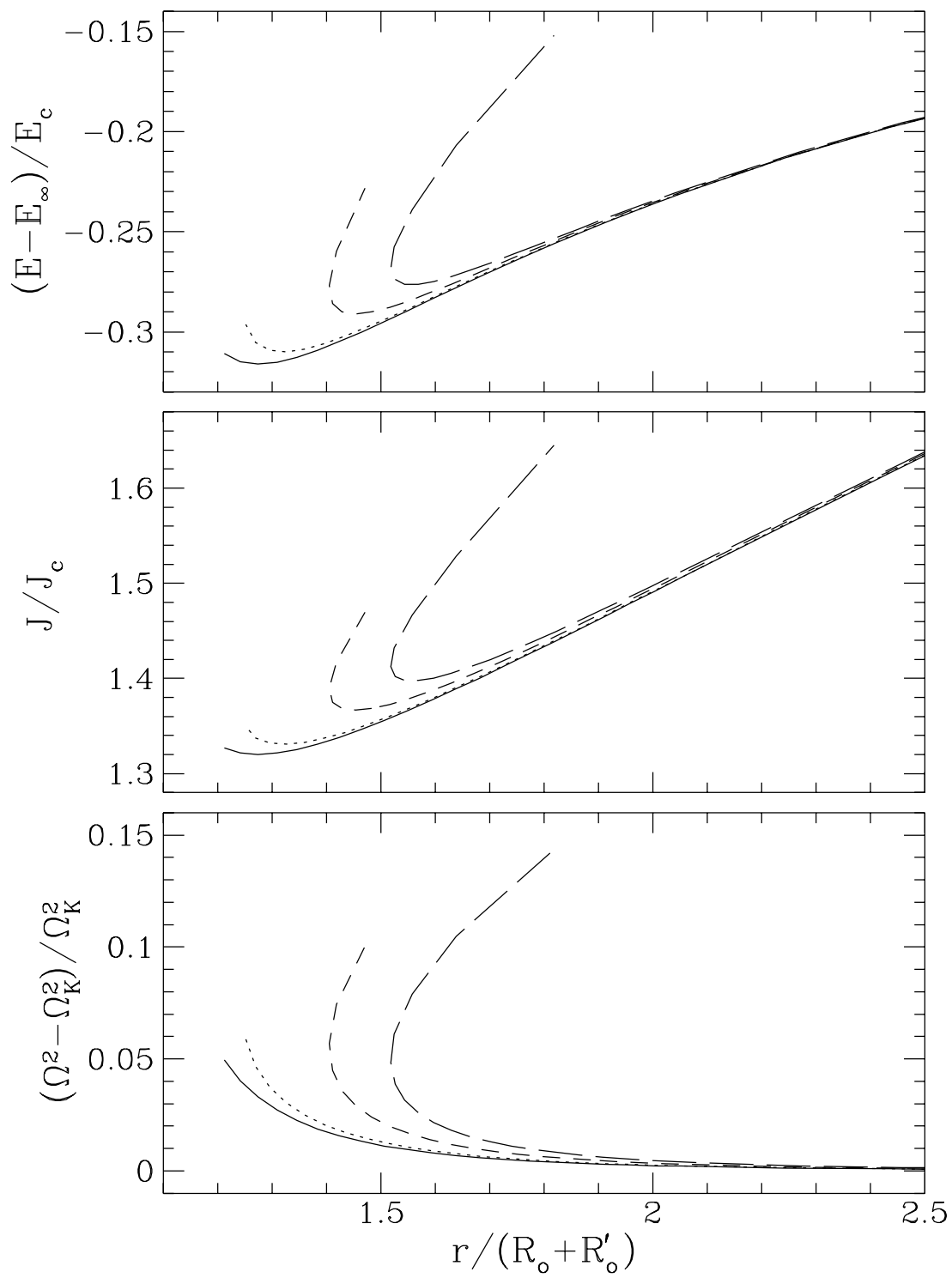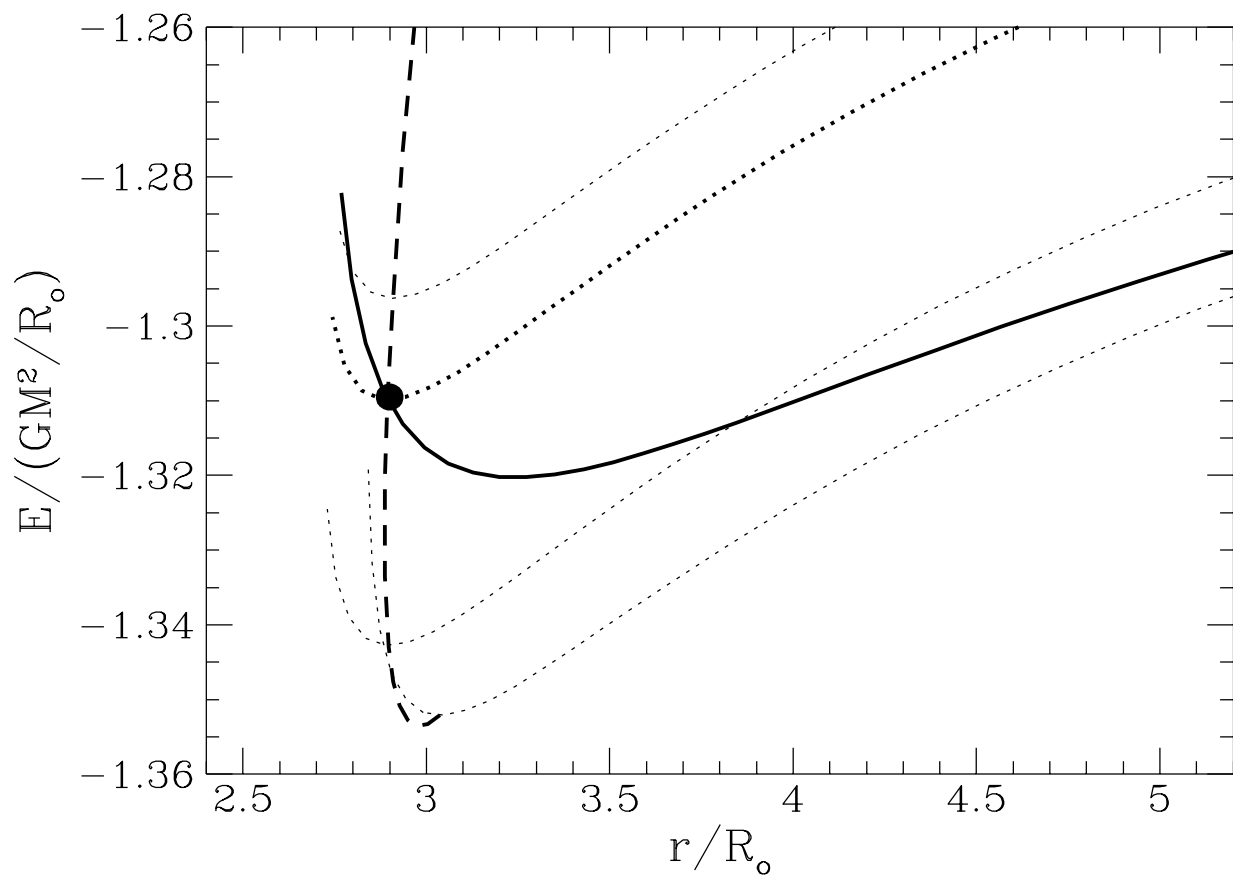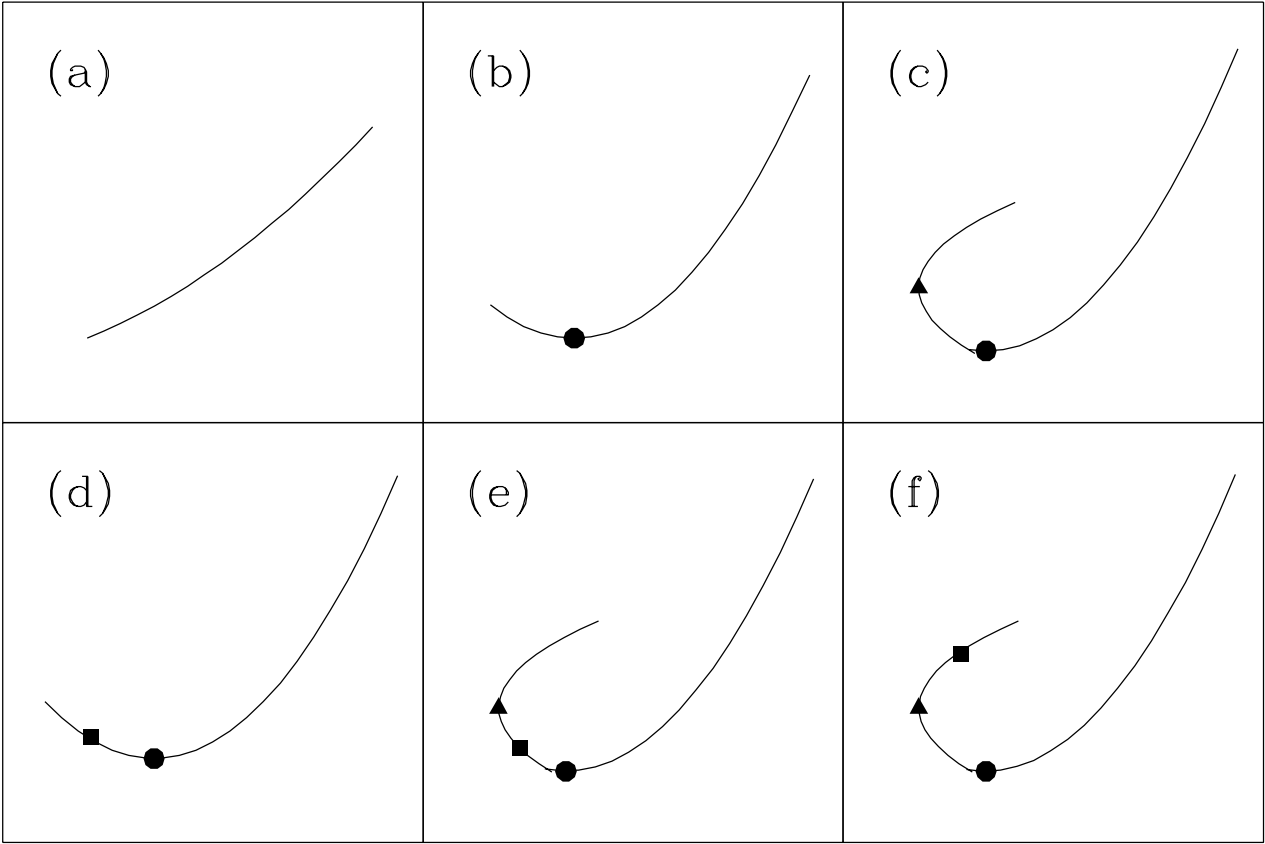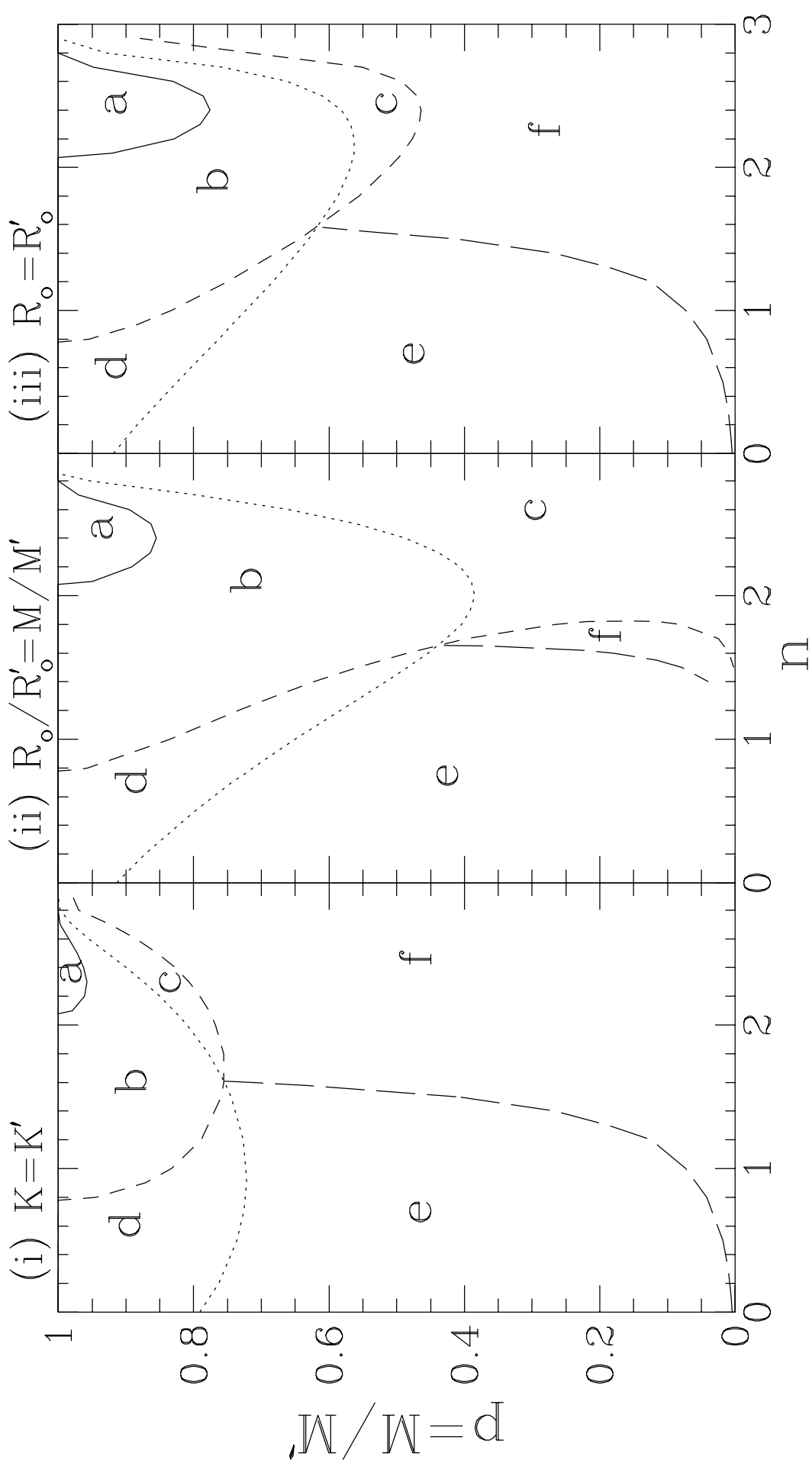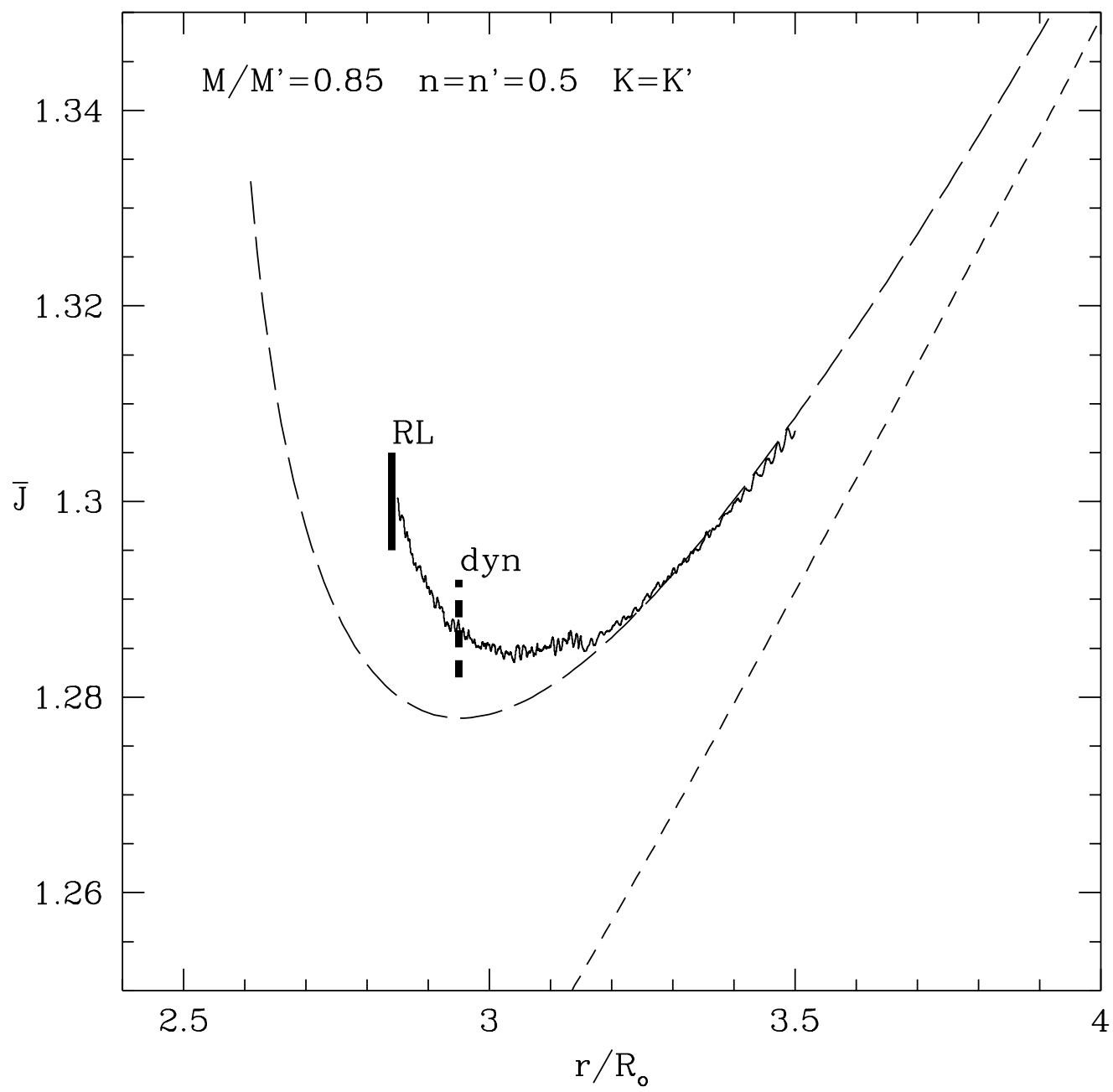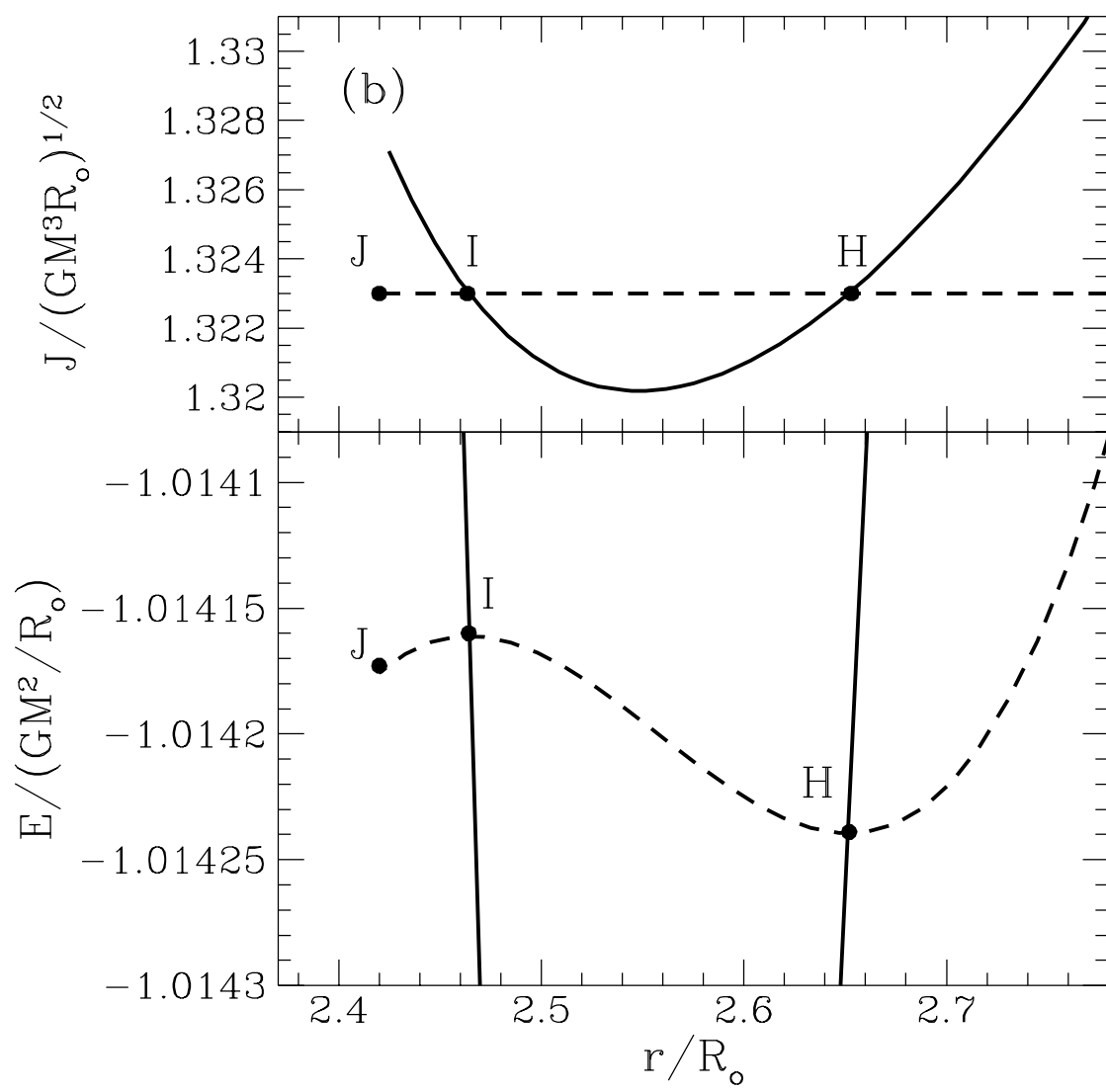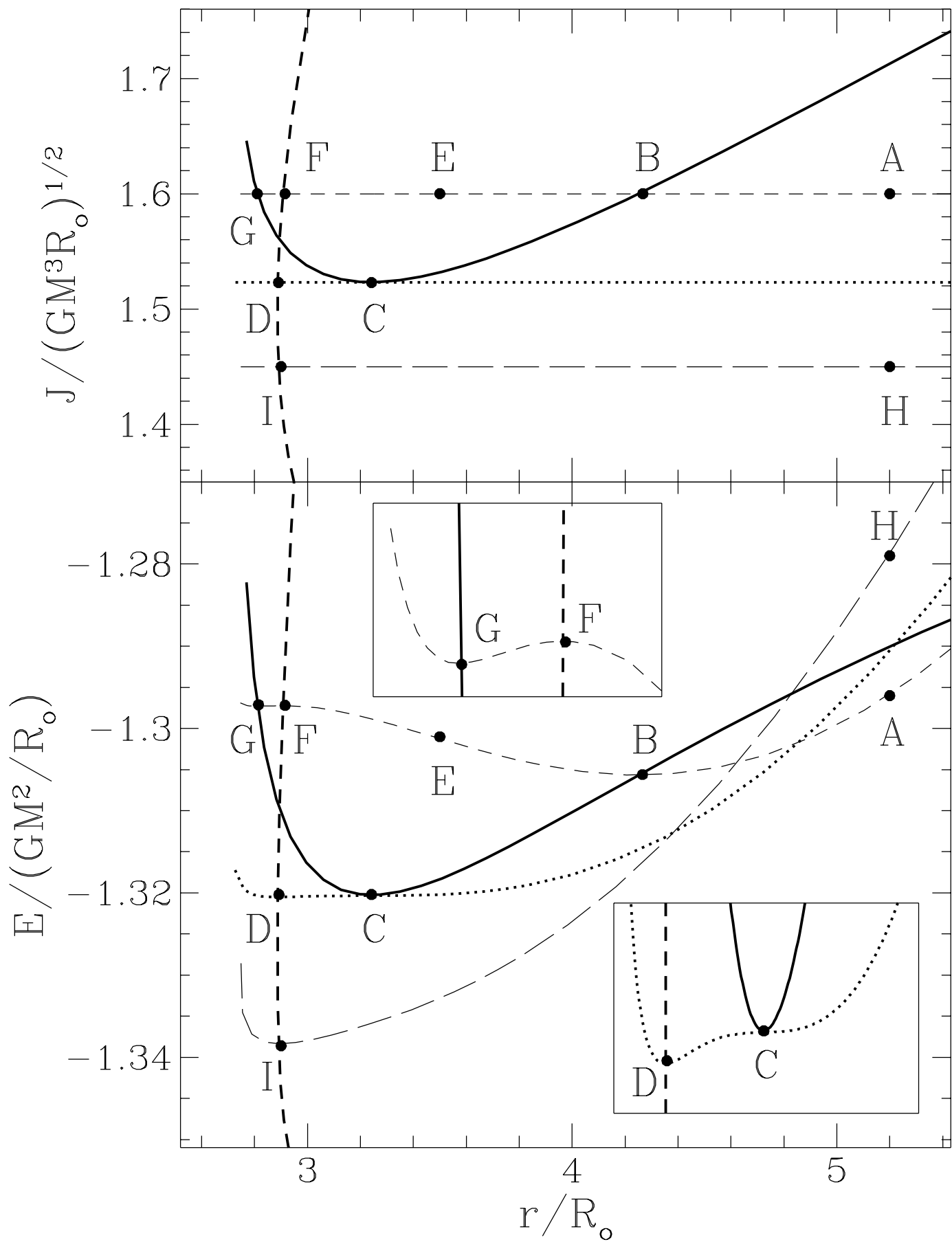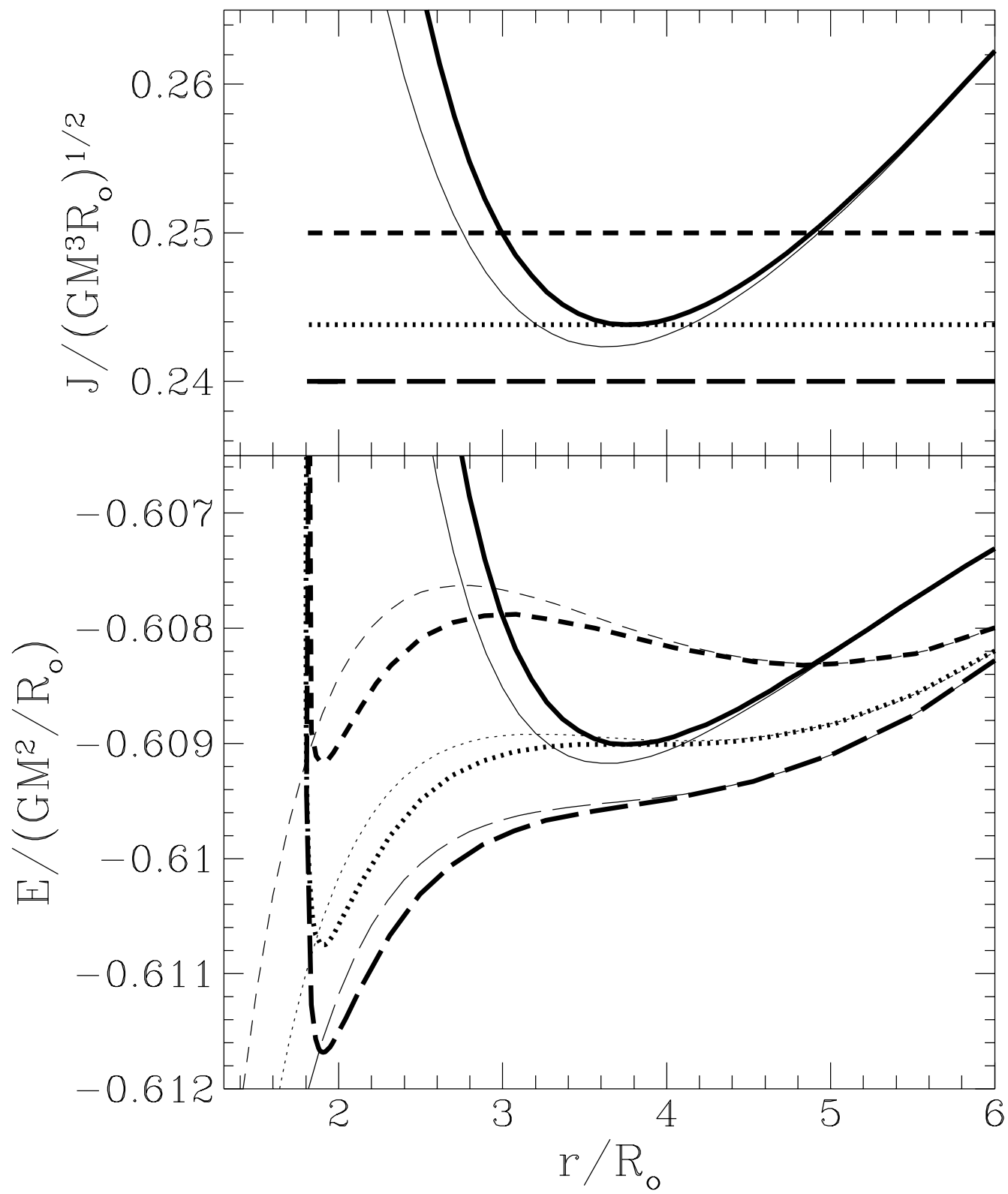
TABLE 1
S_EQUENCES_ OF C_OMPRESSIBLE_ D_ARWIN_ M_ODELS_ [a] WITH $K = K'$

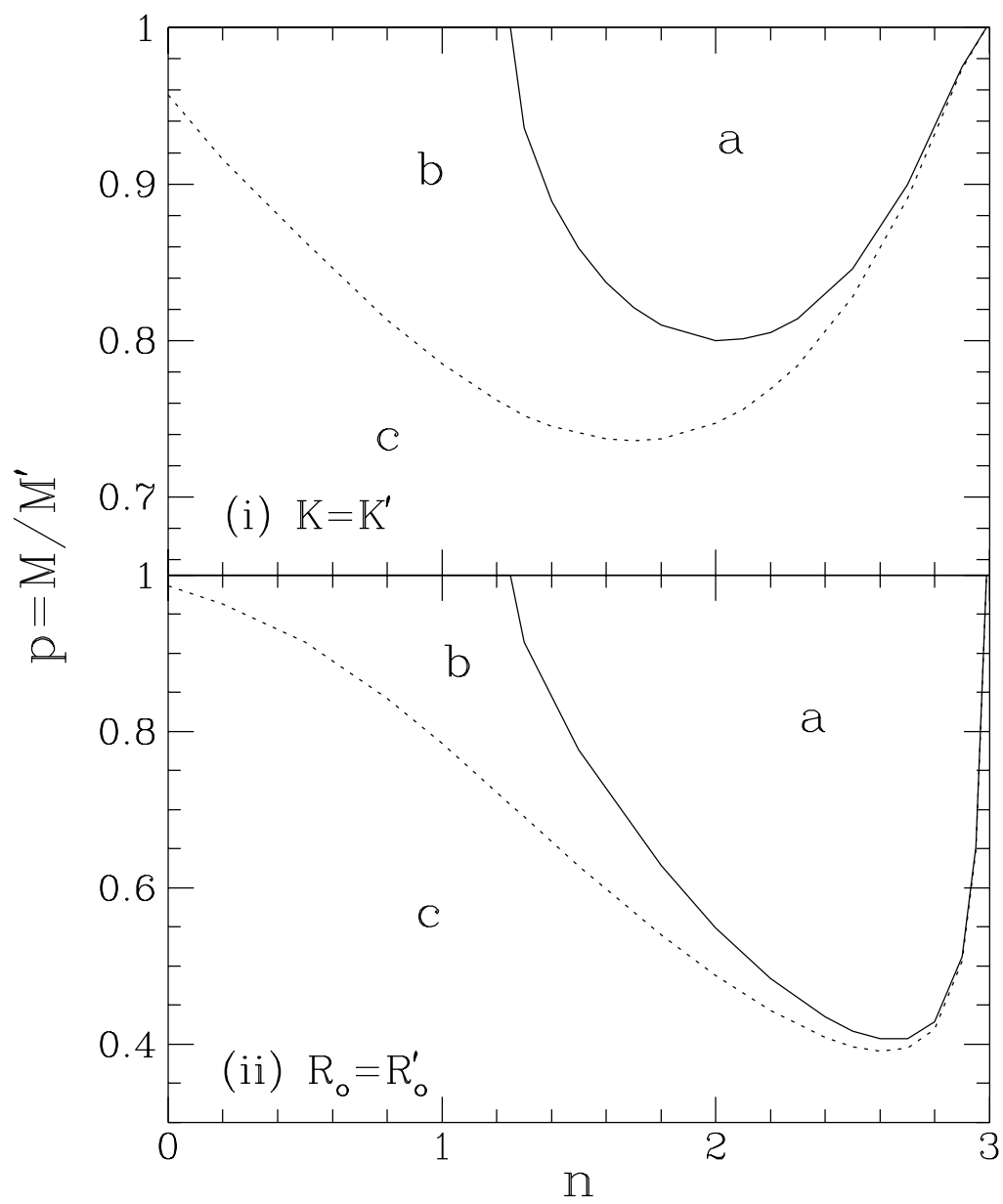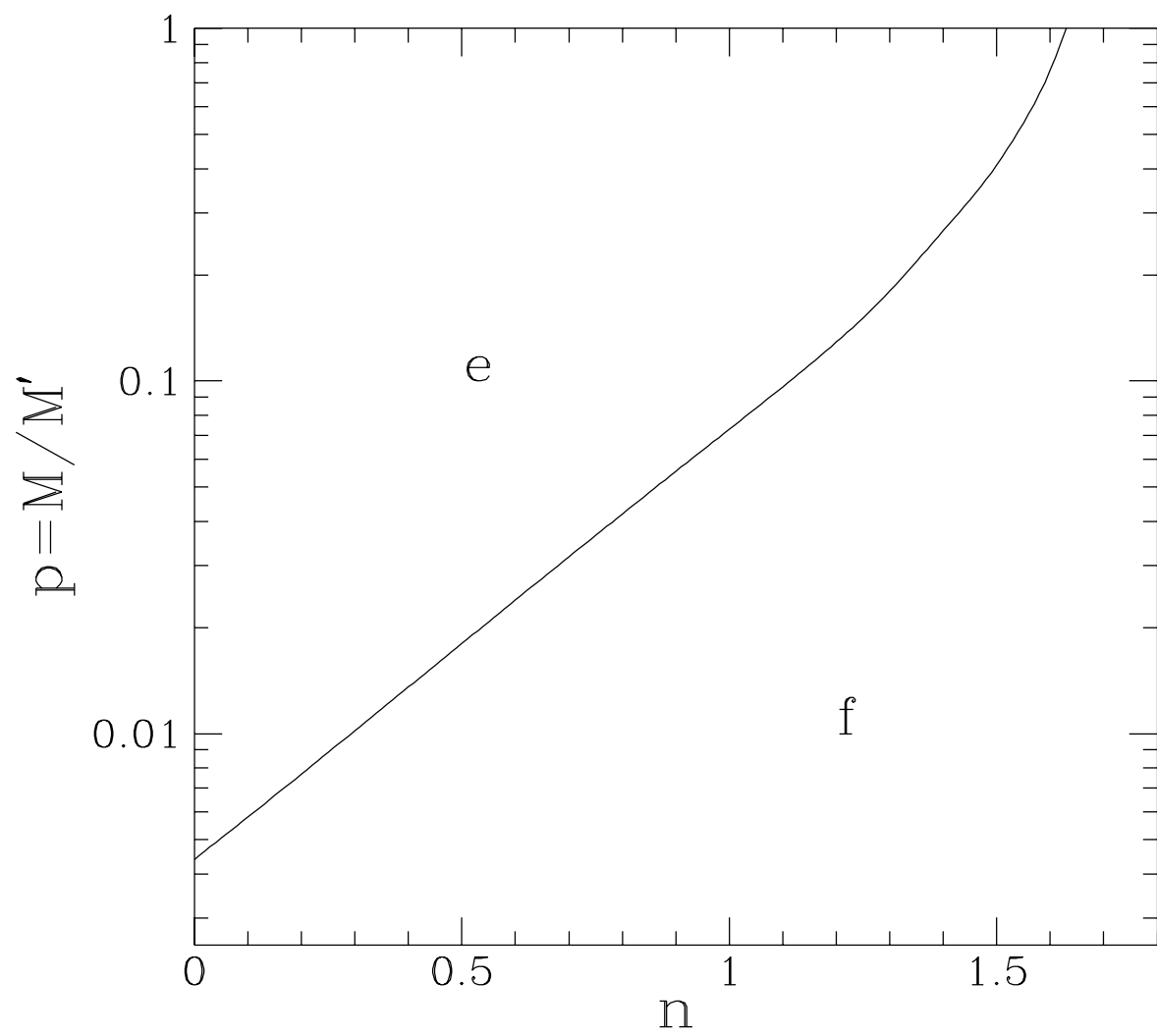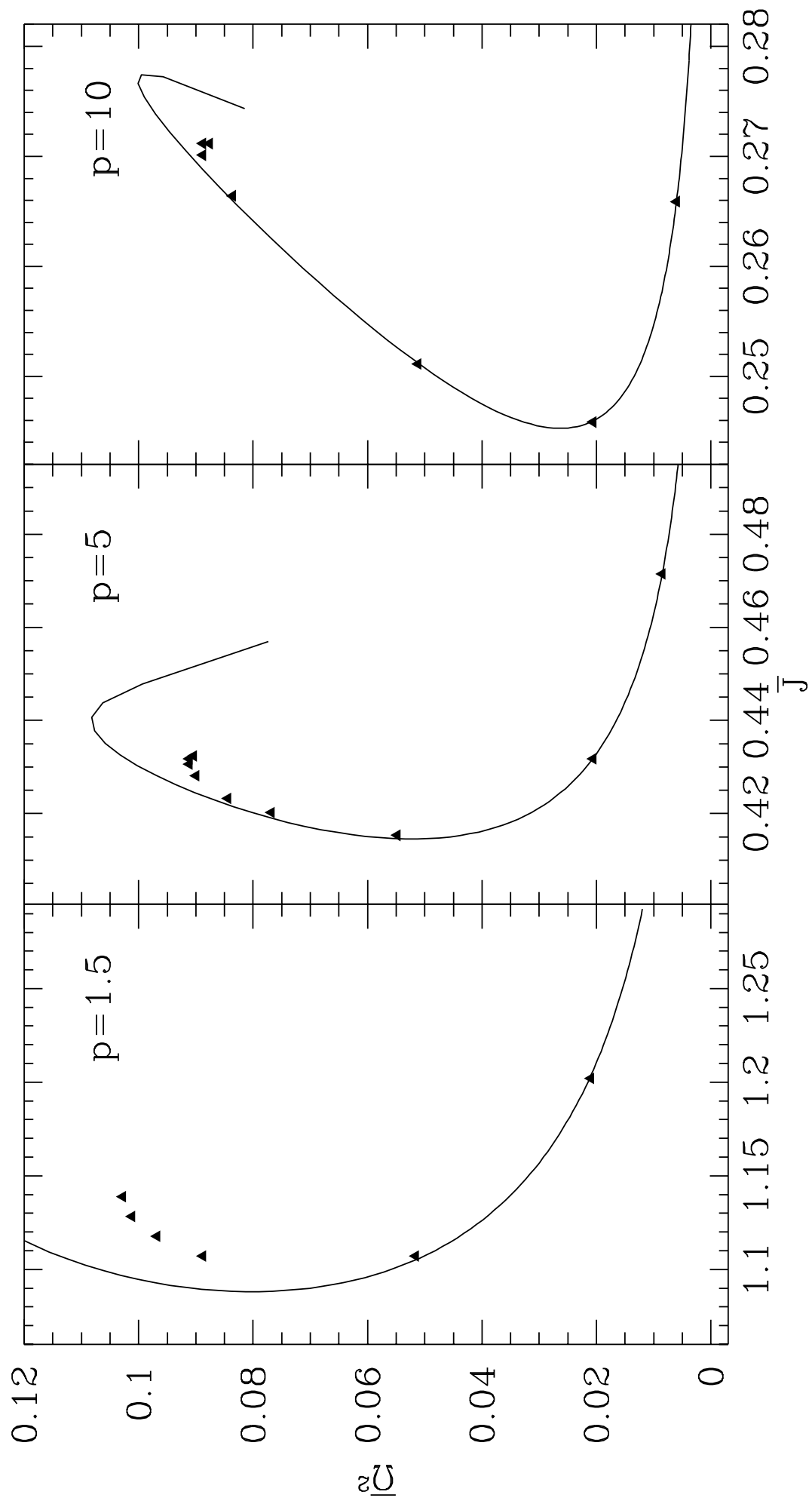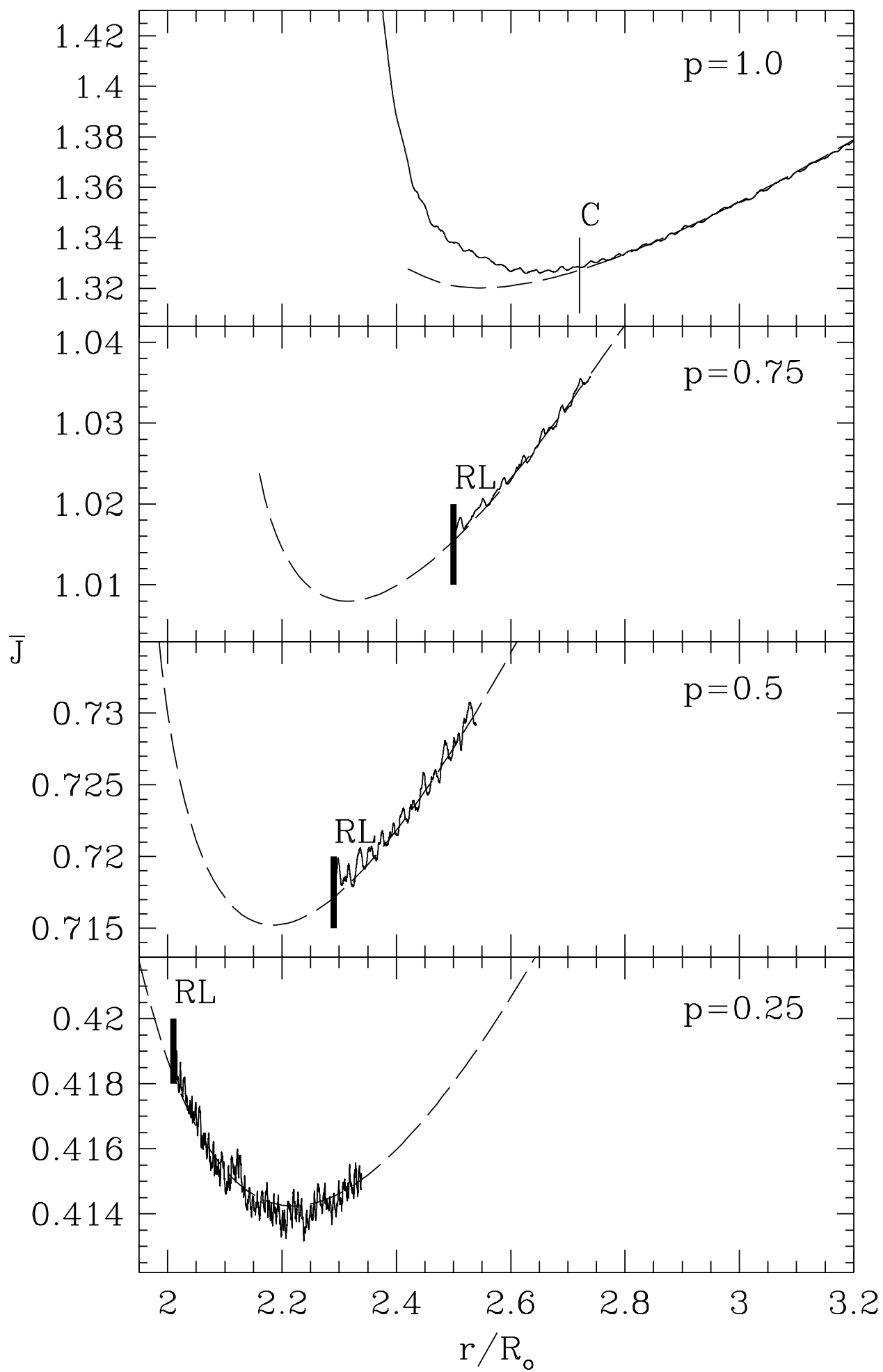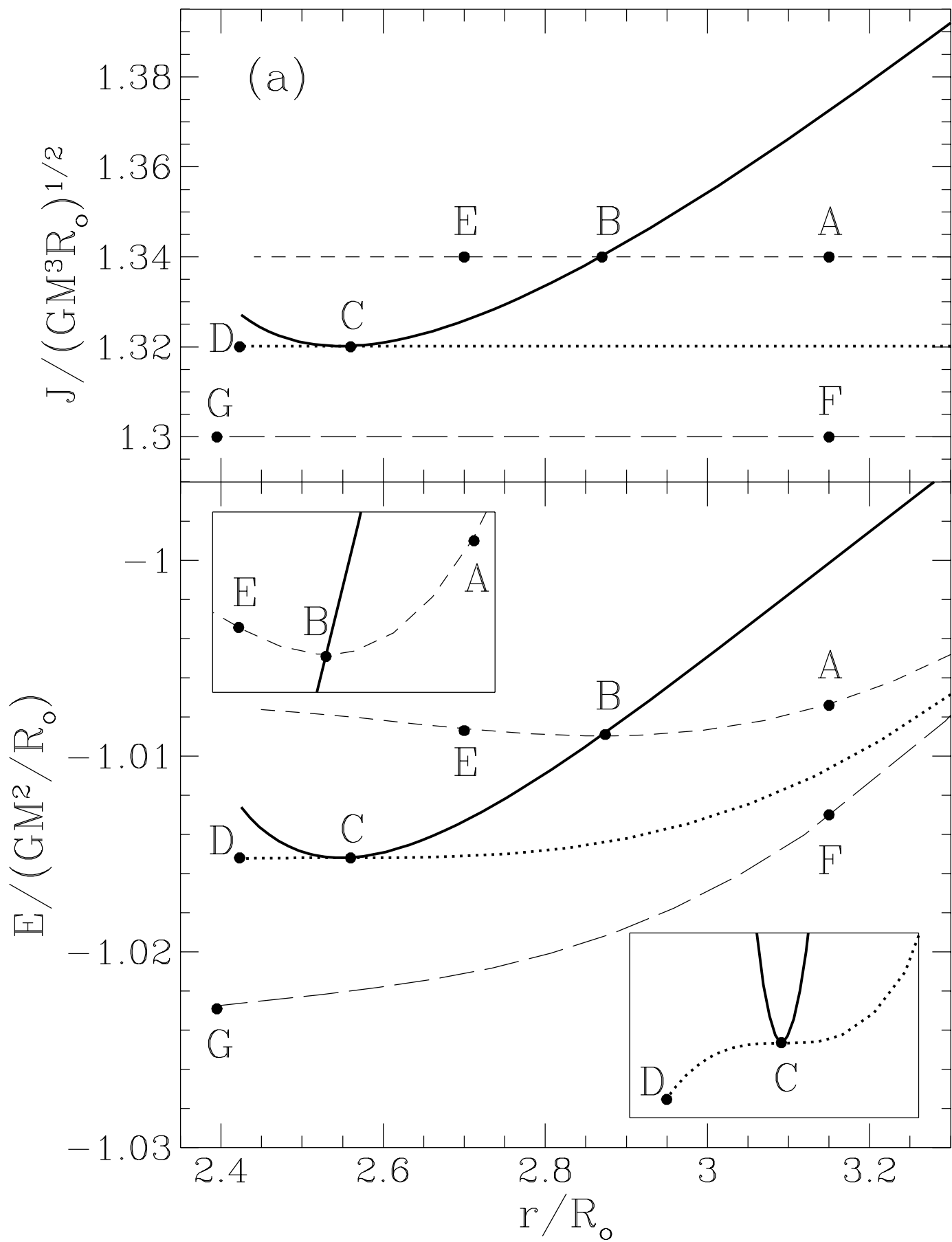| $\hat{r}$ [b]	$\bar{r}$	a_2/a_1	a_3/a_1	R/R_0	a_2'/a_1'	a_3'/a_1'	R'/R_0'	$\bar{\Omega}$	$\bar{J}$	$\bar{E}$
				$n = 0,$	$p = 0.8$					
3.0	3.0459	0.9809	0.9702	1.	0.9847	0.9740	1.	0.1089	2.1913	-1.5645
2.5	2.5656	0.9673	0.9499	1.	0.9739	0.9562	1.	0.1410	2.0496	-1.5797
2.2	2.2841	0.9526	0.9285	1.	0.9621	0.9376	1.	0.1681	1.9686	-1.5905
2.0	2.1012	0.9375	0.9075	1.	0.9501	0.9192	1.	0.1909	1.9190	-1.5982
1.8	1.9239	0.9156	0.8779	1.	0.9328	0.8936	1.	0.2186	1.8762	-1.6058
1.6	1.7552	0.8825	0.8354	1.	0.9067	0.8571	1.	0.2523	1.8453	-1.6120
1.5	1.6755	0.8595	0.8073	1.	0.8888	0.8333	1.	0.2717	1.8371	-1.6139
1.4354*	1.6263	0.8414	0.7860	1.	0.8749	0.8153	1.	0.2852	1.8354	-1.6143
1.3	1.5308	0.7927	0.7310	1.	0.8382	0.7702	1.	0.3157	1.8448	-1.6118
1.2	1.4696	0.7432	0.6786	1.	0.8031	0.7294	1.	0.3397	1.8676	-1.6053
1.1674**	1.4520	0.7236	0.6585	1.	0.7900	0.7148	1.	0.3475	1.8791	-1.6019
1.0	1.3953	0.5693	0.5130	1.	0.7227	0.6428	1.	0.3826	1.9898	-1.5664
				$n = 0,$	$p = 0.5$					
3.0	3.0463	0.9762	0.9653	1.	0.9881	0.9769	1.	0.1108	3.1942	-2.6422
2.5	2.5664	0.9593	0.9416	1.	0.9797	0.9612	1.	0.1434	2.9977	-2.6636
2.0	2.1026	0.9220	0.8920	1.	0.9613	0.9286	1.	0.1941	2.8223	-2.6888
1.8	1.9260	0.8944	0.8572	1.	0.9479	0.9061	1.	0.2221	2.7682	-2.6985
1.6	1.7585	0.8523	0.8069	1.	0.9280	0.8745	1.	0.2560	2.7334	-2.7056
1.5	1.6798	0.8228	0.7733	1.	0.9145	0.8541	1.	0.2754	2.7274	-2.7070
1.4913*	1.6732	0.8198	0.7699	1.	0.9131	0.8522	1.	0.2772	2.7274	-2.7070
1.4	1.6062	0.7848	0.7317	1.	0.8979	0.8302	1.	0.2964	2.7326	-2.7057
1.3	1.5398	0.7346	0.6793	1.	0.8780	0.8025	1.	0.3185	2.7531	-2.7002
1.2049**	1.4871	0.6695	0.6147	1.	0.8566	0.7741	1.	0.3394	2.7929	-2.6888
1.15	1.4646	0.6197	0.5674	1.	0.8449	0.7589	1.	0.3504	2.8286	-2.6781
1.0907***	1.4533	0.5478	0.5014	1.	0.8369	0.7480	1.	0.3588	2.8839	-2.6611
				$n = 0,$	$p = 0.2$					
3.0	3.0484	0.9654	0.9530	1.	0.9931	0.9799	1.	0.1192	6.5239	-9.6405
2.5	2.5697	0.9405	0.9209	1.	0.9882	0.9664	1.	0.1542	6.2472	-9.6728
2.2	2.2901	0.9132	0.8869	1.	0.9829	0.9522	1.	0.1835	6.1235	-9.6907
2.0	2.1093	0.8850	0.8531	1.	0.9775	0.9385	1.	0.2080	6.0732	-9.6992
1.8567*	1.9840	0.8568	0.8205	1.	0.9723	0.9256	1.	0.2285	6.0609	-9.7015
1.8	1.9358	0.8431	0.8051	1.	0.9698	0.9197	1.	0.2373	6.0631	-9.7010
1.6	1.7746	0.7778	0.7341	1.	0.9586	0.8940	1.	0.2719	6.1129	-9.6899
1.5	1.7020	0.7304	0.6851	1.	0.9515	0.8785	1.	0.2908	6.1688	-9.6762
1.4	1.6393	0.6667	0.6220	1.	0.9436	0.8618	1.	0.3096	6.2506	-9.6549
1.3246**	1.6038	0.6016	0.5598	1.	0.9380	0.8504	1.	0.3221	6.3313	-9.6328
1.3	1.5961	0.5757	0.5356	1.	0.9367	0.8474	1.	0.3253	6.3613	-9.6244
1.2621***	1.5908	0.5288	0.4922	1.	0.9355	0.8447	1.	0.3286	6.4111	-9.6103
				$n = 0.5,$	$p = 0.8$					
3.0	3.0367	0.9853	0.9769	1.0010	0.9893	0.9815	1.0009	0.1119	2.1535	-1.4826
2.5	2.5527	0.9747	0.9609	1.0017	0.9816	0.9687	1.0015	0.1453	2.0053	-1.4989
2.0	2.0817	0.9513	0.9267	1.0033	0.9647	0.9416	1.0029	0.1977	1.8623	-1.5199
1.8	1.9004	0.9339	0.9025	1.0046	0.9523	0.9225	1.0040	0.2272	1.8113	-1.5292
1.6	1.7263	0.9072	0.8669	1.0067	0.9336	0.8948	1.0056	0.2633	1.7689	-1.5382
1.5	1.6432	0.8885	0.8430	1.0082	0.9208	0.8765	1.0068	0.2844	1.7531	-1.5419
1.4	1.5639	0.8644	0.8134	1.0102	0.9046	0.8542	1.0083	0.3076	1.7427	-1.5446
1.3194*	1.5036	0.8398	0.7843	1.0125	0.8886	0.8328	1.0099	0.3278	1.7397	-1.5454
1.3	1.4896	0.8330	0.7764	1.0131	0.8843	0.8271	1.0103	0.3328	1.7399	-1.5453
1.2	1.4225	0.7909	0.7293	1.0172	0.8588	0.7948	1.0128	0.3597	1.7481	-1.5428
1.0787**	1.3561	0.7162	0.6516	1.0253	0.8212	0.7493	1.0169	0.3926	1.7813	-1.5320
1.0	1.3300	0.6410	0.5791	1.0347	0.7984	0.7225	1.0196	0.4105	1.8260	-1.5164

TABLE 1 — *continued*

$\hat{r}$ [b]	$\bar{r}$	a_2/a_1	a_3/a_1	R/R_0	a_2'/a_1'	a_3'/a_1'	R'/R_0'	$\bar{\Omega}$	$\bar{J}$	$\bar{E}$
				$n = 0.5,$	$p = 0.5$					
3.0	3.0391	0.9796	0.9701	1.0011	0.9923	0.9850	1.0008	0.1199	3.0766	-2.6367
2.5	2.5562	0.9649	0.9494	1.0020	0.9869	0.9746	1.0014	0.1555	2.8721	-2.6608
2.0	2.0876	0.9322	0.9052	1.0040	0.9751	0.9528	1.0027	0.2112	2.6786	-2.6911
1.8	1.9082	0.9075	0.8737	1.0057	0.9666	0.9377	1.0036	0.2422	2.6121	-2.7041
1.6	1.7373	0.8694	0.8272	1.0085	0.9541	0.9163	1.0050	0.2799	2.5598	-2.7159
1.5	1.6568	0.8422	0.7955	1.0107	0.9458	0.9024	1.0059	0.3015	2.5423	-2.7202
1.4	1.5813	0.8067	0.7558	1.0138	0.9358	0.8862	1.0071	0.3248	2.5336	-2.7226
1.3763*	1.5644	0.7966	0.7448	1.0147	0.9331	0.8820	1.0074	0.3305	2.5332	-2.7227
1.3	1.5134	0.7589	0.7048	1.0183	0.9241	0.8678	1.0084	0.3491	2.5377	-2.7214
1.2	1.4584	0.6917	0.6370	1.0255	0.9119	0.8489	1.0099	0.3727	2.5614	-2.7139
1.1741**	1.4476	0.6694	0.6153	1.0282	0.9090	0.8445	1.0103	0.3780	2.5723	-2.7103
1.1029**	1.4322	0.5926	0.5430	1.0385	0.9043	0.8365	1.0110	0.3886	2.6192	-2.6947
				$n = 0.5,$	$p = 0.2$					
3.5	3.5376	0.9762	0.9675	1.0011	0.9975	0.9927	1.0005	0.1158	6.2701	-10.9014
3.0	3.0513	0.9623	0.9490	1.0017	0.9961	0.9886	1.0008	0.1446	5.9372	-10.9387
2.5	2.5746	0.9349	0.9138	1.0032	0.9935	0.9810	1.0014	0.1868	5.6233	-10.9832
2.2	2.2976	0.9045	0.8765	1.0049	0.9907	0.9731	1.0020	0.2218	5.4597	-11.0120
2.0	2.1198	0.8729	0.8391	1.0070	0.9879	0.9656	1.0025	0.2506	5.3711	-11.0301
1.8	1.9519	0.8252	0.7853	1.0104	0.9842	0.9555	1.0033	0.2844	5.3098	-11.0442
1.6375*	1.8286	0.7664	0.7225	1.0153	0.9804	0.9453	1.0041	0.3149	5.2910	-11.0489
1.6	1.8029	0.7491	0.7046	1.0170	0.9794	0.9428	1.0043	0.3221	5.2922	-11.0486
1.5	1.7426	0.6925	0.6477	1.0228	0.9768	0.9361	1.0049	0.3404	5.3092	-11.0437
1.4050**	1.7044	0.6191	0.5768	1.0317	0.9749	0.9309	1.0053	0.3541	5.3508	-11.0311
1.4	1.7032	0.6147	0.5726	1.0323	0.9749	0.9307	1.0054	0.3546	5.3540	-11.0302
1.3607***	1.6985	0.5752	0.5355	1.0380	0.9746	0.9297	1.0054	0.3574	5.3835	-11.0211
				$n = 1.5,$	$p = 0.8$					
3.0	3.0245	0.9913	0.9863	1.0028	0.9956	0.9924	1.0018	0.1230	2.0585	-1.2546
2.5	2.5353	0.9851	0.9766	1.0049	0.9925	0.9870	1.0030	0.1603	1.9032	-1.2735
2.2	2.2456	0.9781	0.9660	1.0072	0.9890	0.9812	1.0044	0.1924	1.8078	-1.2880
2.0	2.0552	0.9709	0.9552	1.0097	0.9855	0.9753	1.0059	0.2198	1.7443	-1.2993
1.8	1.8684	0.9601	0.9394	1.0135	0.9804	0.9668	1.0080	0.2537	1.6822	-1.3120
1.6	1.6869	0.9433	0.9155	1.0196	0.9727	0.9543	1.0112	0.2962	1.6238	-1.3259
1.5	1.5993	0.9312	0.8989	1.0242	0.9674	0.9458	1.0135	0.3212	1.5972	-1.3329
1.4	1.5146	0.9153	0.8777	1.0304	0.9608	0.9354	1.0164	0.3491	1.5737	-1.3398
1.3	1.4342	0.8940	0.8502	1.0392	0.9525	0.9227	1.0201	0.3798	1.5546	-1.3458
1.2	1.3599	0.8645	0.8138	1.0520	0.9424	0.9073	1.0247	0.4130	1.5423	-1.3500
1.1406*	1.3201	0.8410	0.7861	1.0628	0.9354	0.8970	1.0280	0.4331	1.5400	-1.3508
1.0	1.2518	0.7531	0.6901	1.1090	0.9198	0.8739	1.0359	0.4753	1.5618	-1.3421
				$n = 1.5,$	$p = 0.5$					
3.0	3.0366	0.9827	0.9746	1.0047	0.9979	0.9958	1.0011	0.1574	2.7593	-2.7676
2.5	2.5532	0.9701	0.9566	1.0084	0.9965	0.9930	1.0019	0.2042	2.5560	-2.7992
2.2	2.2695	0.9560	0.9372	1.0127	0.9949	0.9899	1.0027	0.2438	2.4330	-2.8229
2.0	2.0851	0.9413	0.9174	1.0173	0.9934	0.9870	1.0035	0.2770	2.3527	-2.8410
1.8	1.9073	0.9192	0.8885	1.0247	0.9913	0.9829	1.0047	0.3170	2.2767	-2.8605
1.7	1.8222	0.9037	0.8690	1.0302	0.9900	0.9803	1.0054	0.3399	2.2418	-2.8704
1.6	1.7408	0.8840	0.8448	1.0375	0.9884	0.9773	1.0063	0.3645	2.2103	-2.8800
1.5	1.6649	0.8582	0.8142	1.0477	0.9867	0.9739	1.0073	0.3905	2.1840	-2.8886
1.4	1.5973	0.8237	0.7750	1.0625	0.9848	0.9703	1.0083	0.4168	2.1660	-2.8949
1.3267*	1.5563	0.7905	0.7387	1.0780	0.9834	0.9676	1.0091	0.4349	2.1611	-2.8966
1.3	1.5439	0.7763	0.7235	1.0852	0.9830	0.9668	1.0094	0.4408	2.1619	-2.8963
1.1973**	1.5178	0.7056	0.6513	1.1247	0.9820	0.9646	1.0101	0.4560	2.1855	-2.8871
1.1939***	1.5178	0.7027	0.6485	1.1265	0.9820	0.9646	1.0101	0.4562	2.1871	-2.8865

[a] Here $p = M/M'$; $\hat{r} \equiv r/(a_1 + a_1')$; $\bar{r}$, $\bar{\Omega}$, $\bar{J}$ and $\bar{E}$ are defined by eq. (4.1); $R = (a_1 a_2 a_3)^{1/3}$, R_o is defined by eq. (2.39), and similarly for R' and R_o'.

[b] * marks the secular stability limit, ** the dynamical stability limit, *** the Roche limit.

TABLE 2

CRITICAL POINTS ALONG COMPRESSIBLE DARWIN SEQUENCES [a] WITH $K = K'$

p		$\hat{r}$	$\bar{r}$	a_2/a_1	a_3/a_1	R/R_0	a'_2/a'_1	a'_3/a'_1	R'/R'_0	$\bar{\Omega}$	$\bar{J}$	$\bar{E}$
						$n = 0$						
1	sec	1.4293	1.6211	0.8573	0.7995	1.	0.8573	0.7995	1.	0.2861	1.5233	-1.3203
	dyn	1.1622	1.4473	0.7556	0.6853	1.	0.7556	0.6853	1.	0.3488	1.5599	-1.3098
0.8	sec	1.4354	1.6263	0.8414	0.7860	1.	0.8749	0.8153	1.	0.2852	1.8354	-1.6143
	dyn	1.1674	1.4520	0.7236	0.6585	1.	0.7900	0.7148	1.	0.3475	1.8791	-1.6019
0.5	sec	1.4913	1.6732	0.8198	0.7699	1.	0.9131	0.8522	1.	0.2772	2.7274	-2.7070
	dyn	1.2049	1.4871	0.6695	0.6147	1.	0.8566	0.7741	1.	0.3394	2.7929	-2.6888
	lim	1.0907	1.4533	0.5478	0.5014	1.	0.8369	0.7480	1.	0.3588	2.8839	-2.6611
0.2	sec	1.8567	1.9840	0.8568	0.8205	1.	0.9723	0.9256	1.	0.2285	6.0609	-9.7015
	dyn	1.3246	1.6038	0.6016	0.5598	1.	0.9380	0.8504	1.	0.3221	6.3313	-9.6328
	lim	1.2621	1.5908	0.5288	0.4922	1.	0.9355	0.8447	1.	0.3286	6.4111	-9.6103
						$n = 0.5$						
1	sec	1.3125	1.4961	0.8641	0.8078	1.0112	0.8641	0.8078	1.0112	0.3221	1.4553	-1.2425
	dyn	1.0573	1.3386	0.7609	0.6909	1.0218	0.7609	0.6909	1.0218	0.3916	1.4949	-1.2298
0.8	sec	1.3194	1.5036	0.8398	0.7843	1.0125	0.8886	0.8328	1.0099	0.3278	1.7397	-1.5454
	dyn	1.0787	1.3561	0.7162	0.6516	1.0253	0.8212	0.7493	1.0169	0.3926	1.7813	-1.5320
0.5	sec	1.3763	1.5644	0.7966	0.7448	1.0147	0.9331	0.8820	1.0074	0.3305	2.5332	-2.7227
	dyn	1.1741	1.4476	0.6694	0.6153	1.0282	0.9090	0.8445	1.0103	0.3780	2.5723	-2.7103
	lim	1.1029	1.4322	0.5926	0.5430	1.0385	0.9043	0.8365	1.0110	0.3886	2.6192	-2.6947
0.2	sec	1.6375	1.8286	0.7664	0.7225	1.0153	0.9804	0.9453	1.0041	0.3149	5.2910	-11.0489
	dyn	1.4050	1.7044	0.6191	0.5768	1.0317	0.9749	0.9309	1.0053	0.3541	5.3508	-11.0311
	lim	1.3607	1.6985	0.5752	0.5355	1.0380	0.9746	0.9297	1.0054	0.3574	5.3835	-11.0211
0.1	sec	2.0668	2.2245	0.8161	0.7785	1.0105	0.9939	0.9726	1.0024	0.2790	9.3721	-36.2146
	dyn	1.6189	1.9497	0.5946	0.5569	1.0340	0.9905	0.9583	1.0037	0.3437	9.5381	-36.1677
	lim	1.5908	1.9474	0.5686	0.5324	1.0378	0.9905	0.9580	1.0037	0.3449	9.5617	-36.1606
						$n = 1.5$						
1	sec	1.1002	1.2742	0.8854	0.8344	1.0470	0.8854	0.8344	1.0470	0.4079	1.3202	-1.0152
0.8	sec	1.1406	1.3201	0.8410	0.7861	1.0628	0.9354	0.8970	1.0280	0.4331	1.5400	-1.3508
0.75	sec	1.1621	1.3454	0.8319	0.7771	1.0658	0.9464	0.9119	1.0238	0.4353	1.6124	-1.4812
	dyn	1.0059	1.2805	0.7241	0.6622	1.1242	0.9349	0.8939	1.0299	0.4761	1.6437	-1.4686
0.7	sec	1.1869	1.3756	0.8232	0.7686	1.0685	0.9561	0.9256	1.0201	0.4365	1.6942	-1.6422
	dyn	1.0385	1.3174	0.7204	0.6600	1.1243	0.9484	0.9128	1.0243	0.4723	1.7236	-1.6304
	lim	1.0304	1.3171	0.7121	0.6517	1.1295	0.9483	0.9126	1.0244	0.4730	1.7280	-1.6286
0.5	sec	1.3267	1.5563	0.7905	0.7387	1.0780	0.9834	0.9676	1.0091	0.4349	2.1611	-2.8966
	dyn	1.1973	1.5178	0.7056	0.6513	1.1247	0.9820	0.9646	1.0101	0.4560	2.1855	-2.8871
	lim	1.1939	1.5178	0.7027	0.6485	1.1265	0.9820	0.9646	1.0101	0.4562	2.1871	-2.8865
0.4	sec	1.4333	1.7008	0.7740	0.7242	1.0827	0.9913	0.9813	1.0056	0.4312	2.5388	-4.4349
	lim	1.3093	1.6700	0.6978	0.6467	1.1250	0.9908	0.9801	1.0060	0.4468	2.5613	-4.4263
	dyn	1.3087	1.6700	0.6974	0.6463	1.1253	0.9908	0.9800	1.0060	0.4468	2.5615	-4.4262
						$n = 2.5$						
0.95	sec	1.0409	1.2380	0.9140	0.8731	1.1767	0.9668	0.9467	1.0650	0.4774	1.2311	-0.6587
0.9	sec	1.1319	1.3396	0.9089	0.8675	1.1844	0.9833	0.9721	1.0327	0.4787	1.2697	-0.7523
	lim	1.0487	1.3191	0.8772	0.8271	1.2654	0.9823	0.9705	1.0348	0.4915	1.2795	-0.7482
0.8	sec	1.3056	1.5669	0.9022	0.8608	1.1912	0.9956	0.9923	1.0089	0.4776	1.3758	-1.0505
	lim	1.2153	1.5487	0.8737	0.8252	1.2623	0.9955	0.9920	1.0093	0.4875	1.3842	-1.0470
	dyn	1.0681	1.6496	0.7924	0.7321	1.5157	0.9963	0.9934	1.0078	0.4478	1.4714	-1.0114
0.7	sec	1.4774	1.8158	0.8962	0.8553	1.1956	0.9990	0.9981	1.0023	0.4752	1.5181	-1.6605
	lim	1.3795	1.7990	0.8701	0.8232	1.2591	0.9989	0.9981	1.0023	0.4830	1.5256	-1.6574
	dyn	1.1954	1.9097	0.7902	0.7326	1.5015	0.9991	0.9984	1.0020	0.4456	1.6144	-1.6215

[a] Here $p = M/M'$; $\hat{r} \equiv r/(a_1 + a'_1)$; $\bar{r}$, $\bar{\Omega}$, $\bar{J}$ and $\bar{E}$ are defined by eq. (4.1); $R = (a_1 a_2 a_3)^{1/3}$, R_o is defined by eq. (2.39), and similarly for R' and R'_o. The three critical points are secular stability limit ("sec"), dynamical stability limit ("dyn") and Roche limit ("lim").

TABLE 3

POLYTROPIC MODEL FOR LOW-MASS MS STARS [a]

$M/M_\odot$	$R/R_\odot$	n_{eff}	κ_n
0.70	0.658	2.82	0.2192
0.60	0.519	2.27	0.3246
0.50	0.413	1.66	0.4697
0.40	0.353	1.56	0.4953
0.30	0.279	1.56	0.4953
0.25	0.238	1.56	0.4953
0.20	0.191	1.54	0.5006
0.15	0.141	1.52	0.5059
0.11	0.093	1.38	0.5437

[a] Based on D'Antona 1987.